



HAL
open science

Topological Analysis of Hydroxyquinoline Derivatives Interacting with Aluminum Cations or with an Al(111) Surface

Yann Bulteau, Christine Lepetit, Corinne Lacaze-Dufaure

► **To cite this version:**

Yann Bulteau, Christine Lepetit, Corinne Lacaze-Dufaure. Topological Analysis of Hydroxyquinoline Derivatives Interacting with Aluminum Cations or with an Al(111) Surface. *Inorganic Chemistry*, 2020, 59 (24), pp.17916-17928. 10.1021/acs.inorgchem.0c01972 . hal-03160722

HAL Id: hal-03160722

<https://hal.science/hal-03160722v1>

Submitted on 5 Mar 2021

HAL is a multi-disciplinary open access archive for the deposit and dissemination of scientific research documents, whether they are published or not. The documents may come from teaching and research institutions in France or abroad, or from public or private research centers.

L'archive ouverte pluridisciplinaire **HAL**, est destinée au dépôt et à la diffusion de documents scientifiques de niveau recherche, publiés ou non, émanant des établissements d'enseignement et de recherche français ou étrangers, des laboratoires publics ou privés.






Open Archive Toulouse Archive Ouverte (OATAO)

OATAO is an open access repository that collects the work of Toulouse researchers and makes it freely available over the web where possible

This is an author's version published in: <http://oatao.univ-toulouse.fr/27515>

Official URL: <https://doi.org/10.1021/acs.inorgchem.0c01972>

To cite this version:

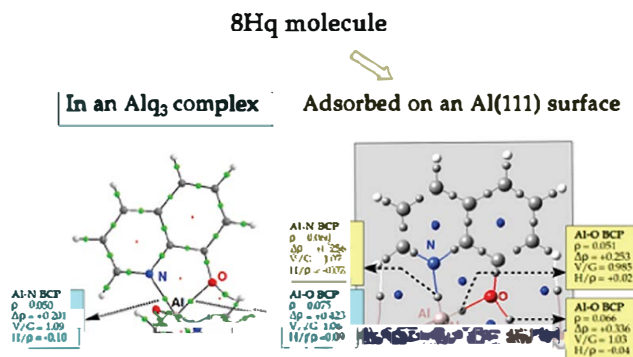
Bulteau, Yann  and Lepetit, Christine  and Lacaze-Dufaure, Corinne 
Topological Analysis of Hydroxyquinoline Derivatives Interacting with Aluminum Cations or with an Al(111) Surface. (2020) *Inorganic Chemistry*, 59 (24). 17916-17928. ISSN 0020-1669

Any correspondence concerning this service should be sent to the repository administrator: tech-oatao@listes-diff.inp-toulouse.fr

Topological Analysis of Hydroxyquinoline Derivatives Interacting with Aluminum Cations or with an Al(111) Surface

Yann Bulteau, Christine Lepetit, and Corinne Lacaze-Dufaure*

ABSTRACT: The reactivity of hydroxyquinoline derivatives (native molecules (Hq) and modified species (HqX, X = Br, SO₃H, or SO₃⁻)) is investigated either (i) with aluminum cations for the formation of chelates or (ii) with aluminum surfaces for their adsorption properties, in the framework of the dispersion corrected Density Functional Theory (DFT D). It is shown that the substituent X has no influence on the complexation to the aluminum cation of the deprotonated active form, i.e., the one exhibiting a phenolate moiety and referred to as q⁻ for the native Hq and qXⁿ⁻ (n = 1 or 2) for its derivatives. The formation energies of the Alq₃ and Al(qX)₃ complexes, taking values of -60.87 ± 3.10 eV in vacuum and -24.30 ± 0.29 eV in water, are indicative of a strong chelating affinity of the q⁻ and qXⁿ⁻ (n = 1 or 2) anions for the aluminum cations. ELF and QTAIM topological analyses on these complexes evidence that the bonding of the deprotonated species with the Al³⁺ ion is ionic with a very weak covalence degree. The *para* or *ortho* substituent X of the phenolate moiety of the qXⁿ⁻ (n = 1 or 2) derivatives modifies the electronic structure only locally and thus does not influence their O or N coordinating properties. The adsorption properties of the latter on an Al(111) surface have also been studied within periodic DFT D calculations. The adsorbed species are strongly interacting with the Al(111) surface, as shown by the value of the adsorption energy of -3.69 ± 0.21 eV for the most stable geometries. Various adsorption modes of the q⁻ and qXⁿ⁻ (n = 1 or 2) derivatives are characterized on the Al surface, depending on stabilizing or destabilizing interactions with the substituents X. On the basis of QTAIM descriptors, the bonding of the hydroxyquinoline species on the aluminum surface is characterized as ionic with a weak covalent character.



1. INTRODUCTION

It is well established that hydroxyquinoline species, i.e., the 8 hydroxyquinoline molecule (Hq), can be used for various applications such as metal cation detection and removal,¹⁻³ organic light emitting diodes (OLEDs),^{4,5} and medicine.⁶ These uses all depend on the chelating ability of the Hq molecule, which is able to complex metal ions leading to highly fluorescent chelates. The Hq molecule was also studied in the perspective of being used as a corrosion inhibitor of aluminum, as the replacement of currently used chromates by environmentally friendly alternatives is required.⁷⁻¹¹

Various derivatives of the Hq molecule have been synthesized, with, for instance, substitution of an H atom by a sulfonic group at the *para* position of the phenyl ring (HqSH in Figure 1 and Table 1). It forms highly soluble fluorescent complexes,^{3,12} and it is used for metal ion detection in aqueous solutions. In addition, electrochemistry studies have shown that this species is an aluminum corrosion accelerator.^{11,13} Another Hq derivative, with Br atoms on the *ortho* and *para* sites of the phenol ring (HqBr in Figure 1 and Table 1), is known for its metal chelating properties. It could be used in the medical field such as other halogen Hq derivatives.⁶ It has

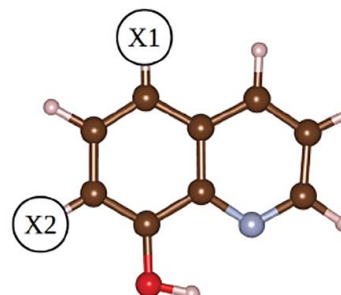


Figure 1. HqX species studied in this work. Substituents X1 and X2 of the phenyl ring are given in Table 1. The oxygen atom is shown in red, the nitrogen atom is shown in blue, carbon atoms are shown in brown, and hydrogen atoms are shown in white.

Table 1. Native Hq and HqX Molecules and Deprotonated q^- and qX^{n-} Anions with Corresponding Groups at X1 and X2 Positions

native	anion	X1	X2
Hq	q^-	H	H
HqBr	qBr^-	Br	Br
HqSH	qSH^-	SO ₃ H	H
HqS	qS^{2-}	SO ₃ ⁻	H

also been tested as a potential corrosion inhibitor of aluminum and showed only very little efficiency.⁸

These applications require stabilization of the organo metallic species and thus strengthening of the interactions of the hydroxyquinoline derivatives (i) with metal ions in order to form chelates and (ii) with metallic surfaces to yield adsorbed Hq species. In the present work, the bonding with aluminum of native and modified Hq molecules, called derivatives (modification at X1 and X2 positions presented in Figure 1), is compared in order to rationalize further chemical modifications. Our first aim is to get insights into the chelating properties of the Hq derivatives. Moreover, to get information in relation to the inhibiting properties of the Hq derivatives, the interaction of the molecules with surfaces is investigated using first principle calculations.¹⁴ It was demonstrated in previous works that the Hq molecule can form stable layers on the Al(111) surface, by direct adsorption of the molecules on the metallic surface^{15–17} or by adsorption of Alq₃ complexes on Al(111).¹⁷ As the bromo and sulfonic Hq modified species showed a weaker inhibiting efficiency than the native Hq, studies of the adsorption of these molecules on aluminum surfaces are required.

The understanding of electronic effects of the substituents on the reactivity of molecules can be addressed using quantum chemistry analysis tools. On the one hand, the simplest approach, called Quantitative Structure Properties Relationship (QSPR), is the deduction of the chemical reactivity of a molecule from descriptors such as the dipole moment and the energy of the frontier orbitals.¹⁸ These descriptors can be calculated by quantum methods, and this approach can be a convenient method to sort a large amount of molecules in a short period of time. However, it has been shown to be of little use concerning complex reactions such as the one involved in corrosion inhibition.¹⁹ On the other hand, accurate analyses of the electronic structure of molecules, obtained by first principles methods, can be performed using topological analyses. For instance, the Quantum Theory of Atoms in Molecules (QTAIM)²⁰ refers to the topological analysis of the electron density partitioning the molecular space into non overlapping atomic basins and yielding atomic charges. The nature of chemical bonds may be characterized from various properties of the electron density at bond critical points. This analysis has been proved useful for the study of metal–ligand bonding.^{21–28} Another approach is the topological analysis of the Electron Localization Function (ELF).^{29,30} It is a unique tool for chemical bonding analysis. It has been successfully used to characterize bonds in molecular^{23–25,31} or periodic extended systems.^{32,33}

In the first part of the present paper, a description of the models and methods used in the molecular or periodic calculations is given in the Computational Details section together with the principles of ELF and QTAIM topological analyses. The results from calculations and topological analyses

of the Hq and HqX molecules and of their Al(qX)₃ complexes are then disclosed in a second part. In the last part, the periodic computations performed in order to evaluate the influence of the substitution in the Hq molecule on its adsorption properties on an Al(111) surface are described.

2. COMPUTATIONAL DETAILS

The hydroxyquinoline molecule studied (Hq) is often referred to as 8 hydroxyquinoline in the literature. The native Hq was studied, together with two derivatives (referred to as HqX in a generic way), namely the 5,7 dibromo 8 hydroxyquinoline molecule (HqBr) and the 8 hydroxyquinoline 5 sulfonic acid (HqSH) presented in Figure 1 and Table 1.

Some of our previous studies had already shown that the deprotonation of the hydroxyl group of the Hq molecule leads to the most reactive species toward aluminum.^{15,16} In the present computational work, we thus investigated the bonding of the deprotonated derivatives (i) with an aluminum atom leading to chelates (molecular computations) and (ii) as a standalone molecule adsorbed on an aluminum surface (periodic computations). The atom numbering for the deprotonated species used hereafter is presented in Figure 2. For clarity, only the C atoms are numbered (C1 to C9).

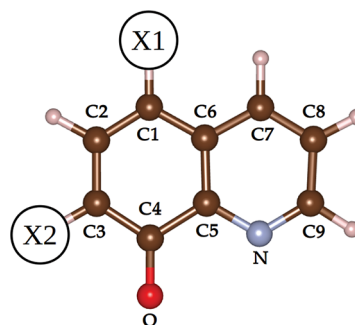


Figure 2. Atom numbering for the deprotonated species studied in this work. Substituents X1 and X2 of the phenyl ring are given in Table 1. The oxygen atom is shown in red, the nitrogen atom is shown in blue, carbon atoms are shown in brown, and hydrogen atoms are shown in white.

2.1. Molecular Calculations and Topological Analysis.

Calculations were first performed on the deprotonated molecules that are anions, i.e., q^- , qBr^- , and qSH^- presented in Table 1, and on aluminum complexes, i.e., Alq₃, Al(qBr)₃, and Al(qSH)₃. Concerning the HqSH molecule, the pK_a of the (SO)₃H/(SO)₃⁻ chemical group has a negative value,³⁴ and the sulfonic group of the molecule is deprotonated in aqueous solution. The qS^{2-} anion and the Al(qS)₃³⁻ complex were thus studied in addition to the qSH^- species. The generic notation of the anions is thus $(qX)^{n-}$ ($n = 1$ or 2) and Al(qX)₃^{m-} ($m = 0$ and 3) for the complexes. However, the charge on the complexes will be omitted hereafter for clarity. The complexes will be thus referred to as Al(qX)₃.

2.1.1. DFT Computations. The structure of free deprotonated q^- and qX^{n-} ($n = 1$ or 2) anions and of their Alq₃ and Al(qX)₃ complexes was calculated in vacuum at the DFT D level. The geometries of the systems were fully optimized without symmetry constraints using conjugate gradient methods with the GAUSSIAN09 package.³⁵ The gradient corrected PBE functional³⁶ was chosen together with the def2TZVP basis set^{37,38} and Grimme's dispersion corrections.^{39,40} All the stationary points were characterized as minima by a vibrational analysis. The calculated total energies included zero point corrections.

The formation energies $E_{\text{form}}^{\text{complex}}$ of the Alq₃ and Al(qX)₃ complexes were calculated in vacuum from the total energies E^{complex} of the complex, E^{mol} of the isolated q^- and qX^{n-} species, and $E^{\text{Al}^{3+}}$ of the aluminum ion, respectively:

$$E_{\text{form}}^{\text{complex}} = E^{\text{complex}} - 3E^{\text{mol}} - E^{\text{Al}^{3+}} \quad (1)$$

The electronic structure of the most stable geometries was analyzed in terms of atomic charges and chemical bonding using ELF and QTAIM topological analyses.

2.1.2. Topological Analyses. Topological methods are based on the analysis of the gradient field of a local function within the dynamic field theory and provide a partition of the molecular space into nonoverlapping basins.

The topological analysis of the electron density ρ designed as the Quantum Theory of Atoms in Molecules (QTAIM) by Bader yields atomic basins and QTAIM atomic charges.²⁰ It allows defining bond paths and bond critical points (BCPs). The nature of the chemical bond is characterized from various properties of the electron density at the BCPs (ρ_{bcp}), especially the sign of the Laplacian of the electron density ($\nabla^2\rho_{\text{bcp}}$) and the values of the kinetic energy density (G_{bcp}), of the potential energy density (V_{bcp}), and of the energy density ($H_{\text{bcp}} = (G_{\text{bcp}}) + (V_{\text{bcp}})$) following Macchi's classification.⁴¹ A negative Laplacian of ρ at the BCP ($\nabla^2\rho_{\text{bcp}} < 0$) corresponds to a local concentration of ρ indicating an electron sharing bond (i.e., covalent bond), while a positive Laplacian ($\nabla^2\rho_{\text{bcp}} > 0$) corresponds to a local depletion of ρ , indicating a closed shell interaction (i.e., ionic bond).

The $\frac{|V_{\text{bcp}}|}{G_{\text{bcp}}}$ descriptor was used by Bianchi et al.²¹ to distinguish three bonding regimes: (i) ionic bonds with $\frac{|V_{\text{bcp}}|}{G_{\text{bcp}}} < 1$, (ii) covalent bonds for $\frac{|V_{\text{bcp}}|}{G_{\text{bcp}}} > 2$, and (iii) an intermediate bonding regime including dative and metal–metal bonds ($1 < \frac{|V_{\text{bcp}}|}{G_{\text{bcp}}} < 2$). The covalence degree may be estimated from $\frac{H_{\text{bcp}}}{\rho_{\text{bcp}}}$.⁴²

The electron localization function (ELF) measures the excess of kinetic energy due to the Pauli repulsion.^{29,30} ELF values are confined between 0 and 1. ELF tends to a value of 1 in those regions where the electron localization is high (atomic shells, chemical bonds, and single electron or lone pairs), whereas it tends toward small values at the boundaries between these regions.^{43,44} The topological analysis of the ELF gradient field yields a partition of the molecular space into nonoverlapping basins of attractors, classified into core, valence bonding, and nonbonding basins. The attractors, namely local maxima of the ELF function, can be single points (general case), circles, or spheres depending on the symmetry. These basins are in one to one correspondence to the core, lone, or shared pairs of the Lewis model. A core basin contains a nucleus X (except a proton) and is designated as C(X). A valence basin lies between two or more core basins. Valence basins are further distinguished by their synaptic order, which is the number of core basins with which they share a common boundary. The monosynaptic basins denoted as V(X), correspond to lone pairs, whereas the di- and polysynaptic ones are related to bi- or multicentric bonds, denoted as V(X1, X2, X3, ...). The average population of the basin is obtained by integration of the one electron density over the basin volume. A statistical population analysis allows for considering the variance and the covariance of the basin populations, which are related to the electron delocalization.⁴⁵ The populations do not take integral values and are about twice the topologically defined Lewis bond orders for bonding valence basins. Electron Localization Function (ELF)^{29,30} topological analyses were performed at the PBE D3/def2TZVP level of calculation, using the TopMoD package.⁴⁶ ELF maps were plotted using the Molekel program.⁴⁷ Quantum Theory of Atoms in Molecules (QTAIM)^{20,48} analyses were performed at the PBE D3/def2TZVP level of calculation, using the AIMAll software.⁴⁹

2.2. Periodic Calculations and Topological Analyses.

Periodic calculations were performed to investigate the adsorption of the molecules on an Al(111) surface. The adsorption of the deprotonated \mathbf{q}^- and \mathbf{qX}^{n-} anions was not investigated, because charged species should be avoided in the framework of periodic calculations. Instead we studied the adsorption of the dehydrogenated molecules, i.e., \mathbf{q} , \mathbf{qBr} , \mathbf{qSH} , and \mathbf{qS} , that are radicals. This method is

usually chosen to study the adsorption of molecules on metallic surfaces resulting in an adsorbed state almost independent of the initial molecule charge.^{50–52}

2.2.1. DFT Computations. Periodic calculations were performed using the Vienna Ab Initio Simulation Package (VASP^{53–55}) with the PAW method.^{56,57} The PBE functional^{58,58} was used for the exchange correlation term. Spin polarization was included. The addition of a dispersion (van der Waals) term to the DFT energy has shown to give more accurate results for organic molecules interacting with a metallic surface in terms of geometry and bonding energy.^{15,16,59} To this end, we used the Grimme's D2 functional.³⁹ All calculations used a cutoff energy (E_{cut}) of 450 eV and a Methfessel Paxton (MP) smearing⁶⁰ with $\sigma = 0.1$ eV. The electronic convergence criterion was 10^{-6} eV. For the geometry optimization, convergence was considered to be reached when the forces on each atom were less than 5×10^{-3} eV·Å⁻¹.

Our aim was to investigate the adsorption properties and bonding of the \mathbf{qX} molecules on the (111) aluminum surface. An asymmetric Al(111) slab of four layers and 30 atoms per layer (6×5 corresponding to a 17.12×14.27 Å² surface area) was used. The two top layers were free to relax, and the two bottom layers were fixed at their bulk positions. On the direction normal to the surface, the vacuum region, that is the distance between the top of the adsorbed species and the bottom of the periodic image of the slab, was larger than 15 Å. A Monkhorst–Pack grid⁶¹ of $3 \times 3 \times 1$ k points was chosen as to have the closest k points density along each dimension, and the convergence of the energy (variation of the energy of less than 0.002 eV) with respect to the number of k points was checked. Finally, dipole correction⁶² to the potential and forces was used to minimize dipole–dipole interaction between image slabs. With the four layers slab and these calculating conditions, a surface energy of 1.19 J/m² was calculated, and it is in very good agreement with the experimental counterpart⁶³ (1.14 J/m²).

The dehydrogenated species were adsorbed on the Al(111) surface at a coverage of 4.62×10^{-3} molecule Å⁻², the maximal surface coverage being 2.36×10^{-2} molecule Å⁻² with all the surface Al atoms covered. The initial positions were chosen to investigate different adsorption topologies and with O and N atoms of the molecules on top, bridge, and 3 fold sites on the Al(111) surface (Figure 3).

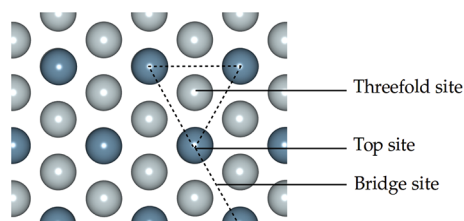


Figure 3. Adsorption sites of the Al(111) surface: 3 fold, top, and bridge sites. Dark blue: surface atoms (layer S). Light blue: subsurface atoms (layers S 1 and S 2).

To get insights in the adsorption process, we calculated the following:

- (i) the adsorption energy of the \mathbf{q} and \mathbf{qX} species on the Al(111) surface:

$$E_{\text{ads}}^{\text{mol}} = E^{\text{slab+mol}} - E^{\text{slab}} - E^{\text{mol}} \quad (2)$$

with $E^{\text{slab+mol}}$ the total energy of the system with \mathbf{q} or \mathbf{qX} adsorbed on the Al(111) surface. E^{slab} and E^{mol} are respectively the energy of the bare relaxed Al(111) slab and of the free \mathbf{q} or \mathbf{qX} molecules optimized in vacuum.

- (ii) the molecule deformation energy:

$$E_{\text{deform}}^{\text{mol}} = E_{\text{SP}}^{\text{mol}} - E^{\text{mol}} \quad (3)$$

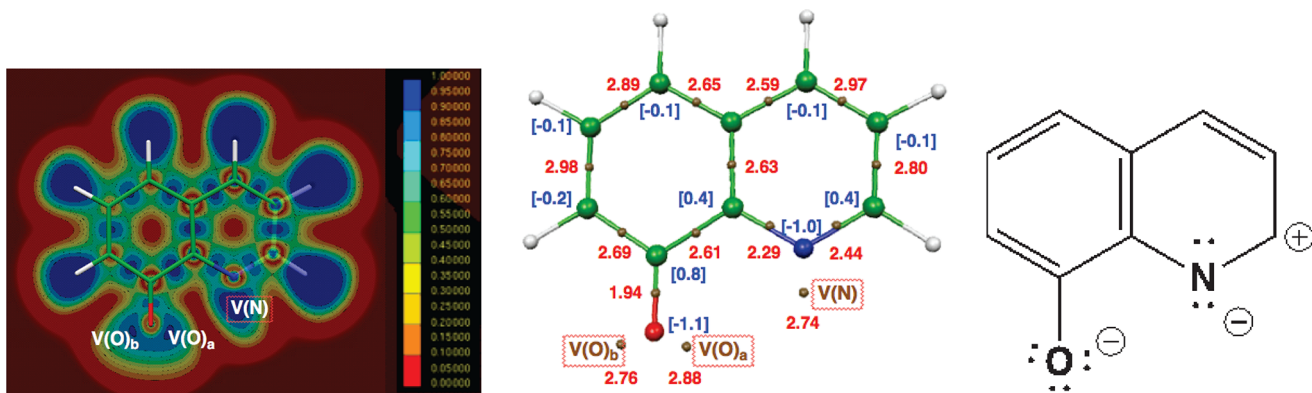


Figure 4. ELF descriptors for the q^- anion. Left: ELF map. Middle: map of ELF attractors (small brown spheres), displaying in red their average populations (in e) and selected QTAIM atomic charges in blue brackets (in e). The oxygen atom is shown in red, the nitrogen atom is shown in blue, carbon atoms are shown in green, and hydrogen atoms are shown in white. Right: phenolate mesomeric form. PBE D3/def2TZVP level of calculation.

with $E_{\text{ads}}^{\text{mol}}$ and E^{mol} respectively the total energy of the isolated molecule at the geometry after adsorption and of the free molecule optimized in vacuum.

(iii) the substrate deformation energy:

$$E_{\text{deform}}^{\text{slab}} = E_{\text{SP}}^{\text{slab}} - E^{\text{slab}} \quad (4)$$

with $E_{\text{SP}}^{\text{slab}}$ and E^{slab} the total energy of the isolated slab at the geometry after adsorption and the total energy of the relaxed slab in vacuum.

(iv) the interaction energy:

$$E_{\text{int}}^{\text{slab/mol}} = E^{\text{slab+mol}} - E_{\text{SP}}^{\text{slab}} - E_{\text{SP}}^{\text{mol}} \quad (5)$$

Figures were plotted using the VESTA code.^{64,65}

2.2.2. Topological Analyses. The QTAIM²⁰ atomic charge Q_x was calculated from the Bader population analysis implemented by Henkelman et al.⁶⁶ for all the atoms of the Al(111) slab and of the q and qX molecules before and after the adsorption process.

Further QTAIM analyses on the optimized geometries of surface adsorbed species were performed using the AIM UC program²⁷ and the Abramov's approximation.⁶⁷ Abramov suggested to calculate the kinetic energy density at the BCPs from $G(r_c) = \left(\frac{3}{10}\right)(3\pi^2)^{2/3}\rho^{5/3}(r_c) + \left(\frac{1}{6}\right)\nabla^2\rho(r_c)$. The local potential energy density can be deduced from an equation derived from the local virial theorem:²⁰ $\left(\frac{1}{3}\right)\nabla^2\rho(r_c) = 2G(r_c) + V(r_c)$.

3. RESULTS AND DISCUSSION

In microelectronic applications, Alq_3 complexes are commonly used as amorphous thin films. When they are present in aqueous solution, they are also suspected to deposit on aluminum surfaces to protect them against corrosion. Similarly, in solution, deprotonated Hq species may also adsorb on the metallic surface to form a protective layer. The bonding of the molecules to aluminum cations or with surface Al atoms is thus of prime interest, and chemical modifications of $blueHq$ could influence this bonding. Hereafter, the structure of the free q^- and qX^{n-} ($n = 1$ or 2) species and Alq_3 and $Al(qX)_3$ complexes in vacuum and the topological analysis of their electronic structure are first presented. Then, the adsorption of q and qX species on Al(111) is investigated and is followed by the determination of the nature and strength of the bonding at the molecule/metal interface.

3.1. Topological Analyses of the Free q^- and qX^{n-} ($n = 1$ or 2) Anions and Their Alq_3 and $Al(qX)_3$ Complexes.

The electronic structures of the q^- and qX^{n-} anions and their aluminum complexes, calculated at the PBE D3/def2TZVP level, were first studied using ELF and QTAIM analyses. The relevant topological descriptors are illustrated first hereafter for the parent q^- anion and further discussed over the series of inhibitors, qBr^- , qSH^- , and qS^2 .

3.1.1. Free q^- and qX^{n-} ($n = 1$ or 2) Species. The map of ELF attractors and their average population is displayed in Figure 4, Table 2, and Table S1 for q^- . It is consistent with

Table 2. Population (in e) of Selected ELF Basins of the q^- and qX^{n-} Anions^a

valence basins	q^-	qBr^-	qSH^-	qS^2
$V(O)_a$	2.88	2.83	2.82	2.92
$V(O)_b$	2.76	2.76	2.79	2.79
$V(C4,O)$	1.94	2.00	2.02	1.88
$V(N)$	2.74	2.72	2.73	2.76
$V(C5,N)$	2.29	2.30	2.27	2.31
$V(C9,N)$	2.44	2.44	2.45	2.43

^aPBE D3/def2TZVP level of calculation.

previous reports of ELF and QTAIM analyses of aromatic compounds among which are naphthalene derivatives^{43,68,69} and of QTAIM descriptors calculated for complexes of hydroxyquinoline with Mn^{III} , Fe^{III} , and Co^{III} .⁷⁰

In previous studies,^{15,16} it was shown that surface Al atoms interact with the deprotonated inhibitor via the O atom of the phenolate moiety and/or the N atom of the pyridine ring. The focus was therefore set on the average population of the ELF monosynaptic $V(O)$ and $V(N)$ basins, that may be related to the lone pairs of the phenolate and amine ligands. According to the local symmetry of the planar q^- anion, the O atom exhibits two inequivalent $V(O)_a$ and $V(O)_b$ ELF basins, while the N atom has only one $V(N)$ basin (Table 2 and Figure 4). For the q^- anion, the populations of $V(O)_a$ and $V(O)_b$ basins add to 5.64 e, thus close to 6 e, while the population of the disynaptic $V(C4,O)$ basin related to the C4–O bond is close to 2 e, in agreement with the phenolate mesomeric form of Figure 4. The population of the $V(N)$ basin is much larger (2.74 e) than the expected value of 2 e, and the population of the disynaptic basins $V(C5,N)$ and $V(C9,N)$ respectively 2.29 and 2.44 e is much lower than the 3 e value expected for an aromatic C–N

bond, suggesting that the weight of the pyridine mesomeric form of Figure 4 is significant. All the above population values are however slightly dependent on the substituting group (Table 2), suggesting that the coordinating properties of the phenolate and pyridine ligands of the \mathbf{qX}^{n-} anions will not be dependent on the substituents introduced in X1 and X2 positions.

Similarly the QTAIM atomic charges of O, N, C5, and C9 are almost the same over the anions series, close to -1.1 e, -1.0 e, and -0.8 e (Table S2). This is consistent with the mesomeric form of Figure 4.

3.1.2. Alq_3 and $\text{Al}(\mathbf{qX})_3$ Complexes. The Alq_3 and $\text{Al}(\mathbf{qS})_3$ complexes have already been studied in the literature and can exist in two forms, the fac and mer isomers, differing in the arrangement of O and N atoms around the Al^{3+} ion. The present study was restricted to the mer isomer (Figure 5), more stable by 138 meV (this work) and 135 meV³ than the fac isomer for Alq_3 and $\text{Al}(\mathbf{qS})_3$, respectively.

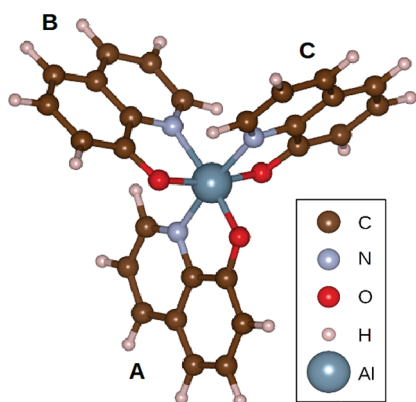


Figure 5. Mer isomer of the Alq_3 complex.

The metal–ligand bond distances of the Alq_3 complex of distorted octahedral symmetry are given in Table 3. The Al–O

Table 3. Bond Lengths (in Å) in the Alq_3 and $\text{Al}(\mathbf{qX})_3$ Complexes^a

	Alq_3	$\text{Al}(\mathbf{qBr})_3$	$\text{Al}(\mathbf{qSH})_3$	$\text{Al}(\mathbf{qS})_3$
A				
$d_{\text{Al-O}}$	1.863	1.860	1.867	1.871
$d_{\text{Al-N}}$	2.058	2.057	2.056	2.066
B				
$d_{\text{Al-O}}$	1.891	1.886	1.890	1.896
$d_{\text{Al-N}}$	2.101	2.100	2.088	2.100
C				
$d_{\text{Al-O}}$	1.894	1.888	1.892	1.899
$d_{\text{Al-N}}$	2.045	2.045	2.042	2.053

^aSee A, B, and C moieties of the complexes in Figure 5. PBE D3/def2TZVP level of calculation.

bond lengths of 1.863, 1.891, and 1.894 Å and Al–N bond lengths of 2.058, 2.101, and 2.045 Å are in accordance with previous BLYP,⁷¹ GGA,⁷² and PBE⁷³ calculations as well as with experimental measurements.^{74,75} The Al–O bond lengths are comparable to the sum of ionic radii of Al and O, i.e., about 1.9 Å, suggesting the formation of three ionic bonds between Al^{3+} and \mathbf{q}^- ions. Similar arrangements of the molecules are found in $\text{Al}(\mathbf{qBr})_3$, $\text{Al}(\mathbf{qSH})_3$, and $\text{Al}(\mathbf{qS})_3$ (Table 3), suggesting that the modification of the substituent on X1

and X2 positions and the deprotonation of the SO_3H group has no influence on the final geometry of the aluminum complex.

The energies of formation of the Alq_3 and $\text{Al}(\mathbf{qX})_3$ complexes in vacuum are given in Table S3. The values are -60.87 ± 3.10 eV and indicate strong interactions between \mathbf{q}^- and \mathbf{qX}^{n-} anions, and the Al^{3+} ion and are consistent with the ionic bonding as it will be shown below. The description of the electronic structure of the complexes was improved to get formation energies in aqueous solution, using Truhlar and co-workers' SMD solvation model⁷⁶ by placing the solute in a cavity within the solvent reaction field. The energies of formation in water converge toward -24.30 ± 0.29 eV for all the complexes, suggesting again similar chelating properties for the \mathbf{q}^- and \mathbf{qX}^{n-} species.

The investigation of the bonding in Alq_3 complexes has been started in a previous work,¹⁷ in the framework of periodic DFT computations. The study of the interactions between dehydrogenated \mathbf{q} species and an Al atom was shown to be in favor of an ionic covalent bonding, but accurate topological analysis was needed to support this conclusion and to quantify the covalent character of the bonding. In the present work, the ELF descriptors calculated for Alq_3 are displayed in Figure 6, Table 4, and Table S1. Only the population of V(O) and V(C4,O) basins of \mathbf{qX}^{n-} , thus the description of the phenolate moieties, is modified upon complexation to Al. Due to strong symmetry reduction, the V(O) basins exhibit very different populations, $V(\text{O})_a = 2.31$ e, $V(\text{O})_b = 3.70$ e, adding to a larger value (6 e) than for the unbonded \mathbf{q}^- anion (5.64 e), while the V(C4,O) basin populations have been concomitantly depleted from 1.94 e down to 1.64 e. The absence of a disynaptic attractor between Al and O or between Al and N is in favor of an ionic bonding between Al^{3+} and the three \mathbf{q}^- anions. The negligible atomic contribution of Al to $V(\text{O})_a$ or to V(N) basins (about 3%) and the very low covariance between C(Al) and V(O) and V(N) basins ($\text{cov}(V(\text{O})_a, \text{C}(\text{Al})) = -0.05$ and $\text{cov}(V(\text{N}), \text{C}(\text{Al})) = -0.04$) are indeed indicative of a very weak covalence degree of the Al–O and Al–N ionic bonds (Table 4).

The same ELF description holds for the other complexes of the series, i.e., $\text{Al}(\mathbf{qBr})_3$, $\text{Al}(\mathbf{qSH})_3$, and $\text{Al}(\mathbf{qS})_3$ complexes. In the case of $\text{Al}(\mathbf{qBr})_3$, the populations of the V(C, Br) and V(Br) basins are also affected by the local symmetry reduction. The population of disynaptic V(C,Br) valence basins is depleted of about 0.13 e. Moreover, the number of monosynaptic V(Br) basins decreases from 3 in the free \mathbf{qBr}^- anion to 2 in the complex.

QTAIM analysis was performed on the four complexes. Selected QTAIM atomic charges are displayed in Table S2 and are very similar over the series. The QTAIM descriptors, i.e., ρ_{bcp} , $\nabla^2 \rho_{\text{bcp}}$, $\frac{|V_{\text{bcp}}|}{G_{\text{bcp}}}$, and $\frac{H_{\text{bcp}}}{\rho_{\text{bcp}}}$, of Al–O and Al–N bond critical points (BCPs) are also very similar over all the series of Al complexes (Figure 7 and Table 5).

The $\frac{|V_{\text{bcp}}|}{G_{\text{bcp}}}$ values slightly larger than 1 point toward the ionic bonding domain at the borderline with the intermediate bonding regime including dative bonding. The weak electron density values and the large positive Laplacian values are also in favor of ionic bonding. Small negative energy densities suggest however a very weak covalence degree as indicated by

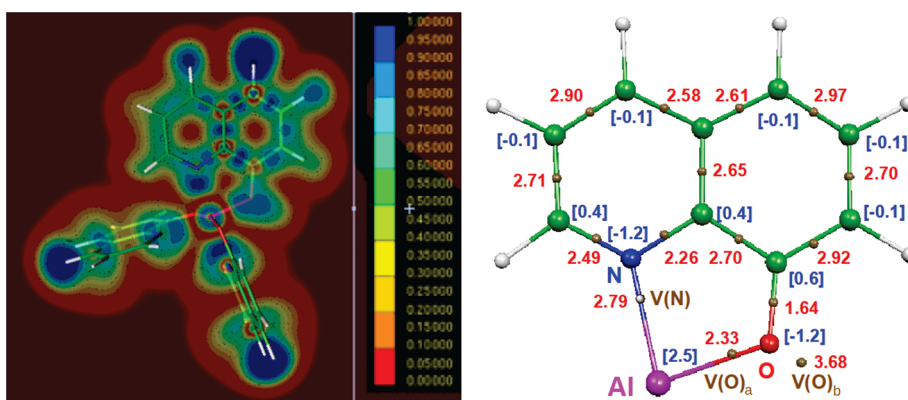


Figure 6. ELF descriptors of the Alq_3 complex. Left: ELF map. Right: partial map of ELF attractors (small brown spheres) restricted to a q^- moiety of Alq_3 , displaying in red their average populations (in e) and selected QTAIM atomic charges in blue brackets (in e). The aluminum atom is shown in magenta, the oxygen atom is shown in red, the nitrogen atom is shown in blue, carbon atoms are shown in green, and hydrogen atoms are shown in white. PBE D3/def2TZVP level of calculation.

Table 4. Relevant ELF Descriptors of the Al–O and Al–N Bonds in Alq_3 and $\text{Al}(q\text{X})_3$ Complexes^a

ELF descriptors	Alq_3	$\text{Al}(q\text{Br})_3$	$\text{Al}(q\text{SH})_3$	$\text{Al}(q\text{S})_3$	$\text{Al}(q\text{CN})_3$	$\text{Al}(q\text{NH}_2)_3$
$V(\text{O})_a$	2.31	2.30	2.34	2.29	2.33	2.26
% Al	3	3	3	3	3	3
$\text{cov}(V(\text{O})_a, C(\text{Al}))$	0.05	0.05	0.05	0.05	0.05	0.05
$V(\text{N})$	2.78	2.80	2.80	2.80	2.79	2.77
% Al	3	3	3	3	3	3
$\text{cov}(V(\text{N}), C(\text{Al}))$	0.04	0.04	0.04	0.04	0.04	0.04

^aDescriptors are averaged over the three quasi equivalent bonds. ELF populations are given in e, $\text{cov}(V(\text{X}), C(\text{Al}))$ refers to the covariance between $V(\text{X})$ and $C(\text{Al})$ basins, and % Al is the QTAIM contribution of Al to $V(\text{O})$ or $V(\text{N})$ basins. PBE D3/def2TZVP level of calculation.

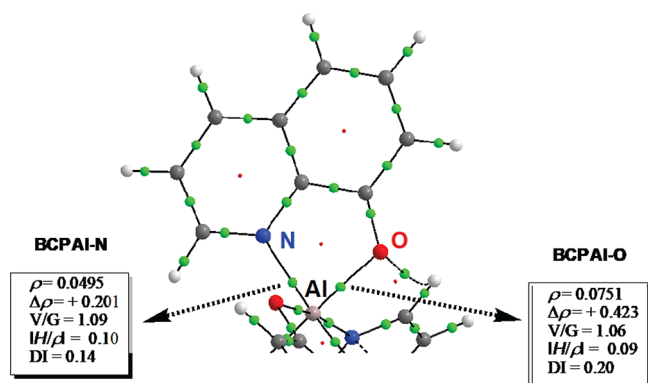


Figure 7. QTAIM molecular graph of Alq_3 restricted to a q^- moiety of the complex (in au).

the $\frac{H_{\text{bcp}}}{\rho_{\text{bcp}}}$ values. This description is consistent with the above ELF analysis.

Although this work focuses on Hq derivatives for which both experimental and computational data are available, topological analysis of two additional Hq derivatives was performed in order to be able to browse the Hammett scale⁷⁷ from the more donating *para* substituent (*p* NH_2 , Hammett constant $\sigma = -0.66$) to the more withdrawing *para* substituent (*p* CN , $\sigma = 0.66$) going through the moderately withdrawing experimental substituents of this work, namely (*p* Br , $\sigma = 0.23$ and *p* SO_3^- , $\sigma = 0.35$). The corresponding data are presented in Table 4 and Table 5 and further supports that the substituent does not have any influence on the Al–O and Al–N bonds of the Alq_3 complexes thus on the complexation of the investigated Hq derivatives. The ELF and QTAIM descriptions of the

interaction of $q\text{X}^n$ ($n = 1$ or 2) anions with aluminum within $\text{Al}(q\text{X})_3$ complexes show no dependence on the *ortho* and *para* substituent of the phenol ring. The Al chelating properties are thus similar for the Hq derivatives studied. This is consistent with the calculated formation energies in aqueous solution that are the same within all the derivatives.

3.2. Topological Analyses of the Charge Density of q and $q\text{X}$ Species Adsorbed on Al(111). Studies of the interaction of q and $q\text{X}$ with an Al(111) surface were then further performed. In contrast to the above Alq_3 and $\text{Al}(q\text{X})_3$ complexes, the interaction with Al atoms is not restricted to the O or N atoms. The underlying hypothesis is then that the interaction of several atoms of $q\text{X}$ with the Al surface atoms could change their properties, as anticipated from the variable efficiencies of the various HqX derivatives toward corrosion inhibition.

3.2.1. Energies and Geometries of the q and $q\text{X}$ Species Adsorbed on Al(111). For each molecule, two adsorption modes were investigated, i.e., a tilted ($q\text{X}^{\text{tilt}}$) and a parallel ($q\text{X}^{\text{paral}}$) adsorption mode. The most stable geometries are presented in Figure 8. For the tilted adsorption mode, the molecules are bound to the surface only by their O and N atoms. The parallel adsorption mode corresponds to a geometry where the molecule is nearly parallel to the surface, with the formation of additional bonds between surface Al atoms and the molecule (mostly by a C atom of the phenol ring or an O atom of the SO_3 and SO_3H groups). Adsorption, deformation, and interaction energies and charge (Q_{mol}) on the adsorbed molecules for each configuration are given in Table 6. For the free $q\text{S}$ species, no stable geometry could be found. Thus, adsorption energy and deformation energy were not calculated. The lengths of the shortest bonds between the

Table 5. Relevant QTAIM Descriptors (in au^a) Related to the Al–O and Al–N Bonds in Alq_3 and $\text{Al}(\text{qX})_3$ Complexes^b

	Alq_3	$\text{Al}(\text{qBr})_3$	$\text{Al}(\text{qSH})_3$	$\text{Al}(\text{qS})_3$	$\text{Al}(\text{qCN})_3$	$\text{Al}(\text{qNH}_2)_3$
BCP Al O						
ρ_{bcp}	0.071	0.072	0.071	0.070	0.071	0.072
$\nabla^2\rho_{\text{bcp}}$	0.397	0.403	0.397	0.388	0.394	0.403
$\frac{ V_{\text{bcp}} }{G_{\text{bcp}}}$	1.06	1.06	1.06	1.06	1.06	1.06
$\frac{H_{\text{bcp}}}{\rho_{\text{bcp}}}$	0.09	0.08	0.08	0.09	0.09	0.09
BCP Al N						
ρ_{bcp}	0.053	0.053	0.054	0.053	0.054	0.052
$\nabla^2\rho_{\text{bcp}}$	0.223	0.223	0.227	0.219	0.226	0.219
$\frac{ V_{\text{bcp}} }{G_{\text{bcp}}}$	1.09	1.09	1.09	1.09	1.09	1.09
$\frac{H_{\text{bcp}}}{\rho_{\text{bcp}}}$	0.10	0.11	0.11	0.11	0.11	0.10

^a ρ_{bcp} in e/bohr^3 , V_{bcp} , G_{bcp} , and H_{bcp} in hartree/bohr³. ^bDescriptors are averaged over the three equivalent bonds. PBE D3/def2TZVP level of calculation.

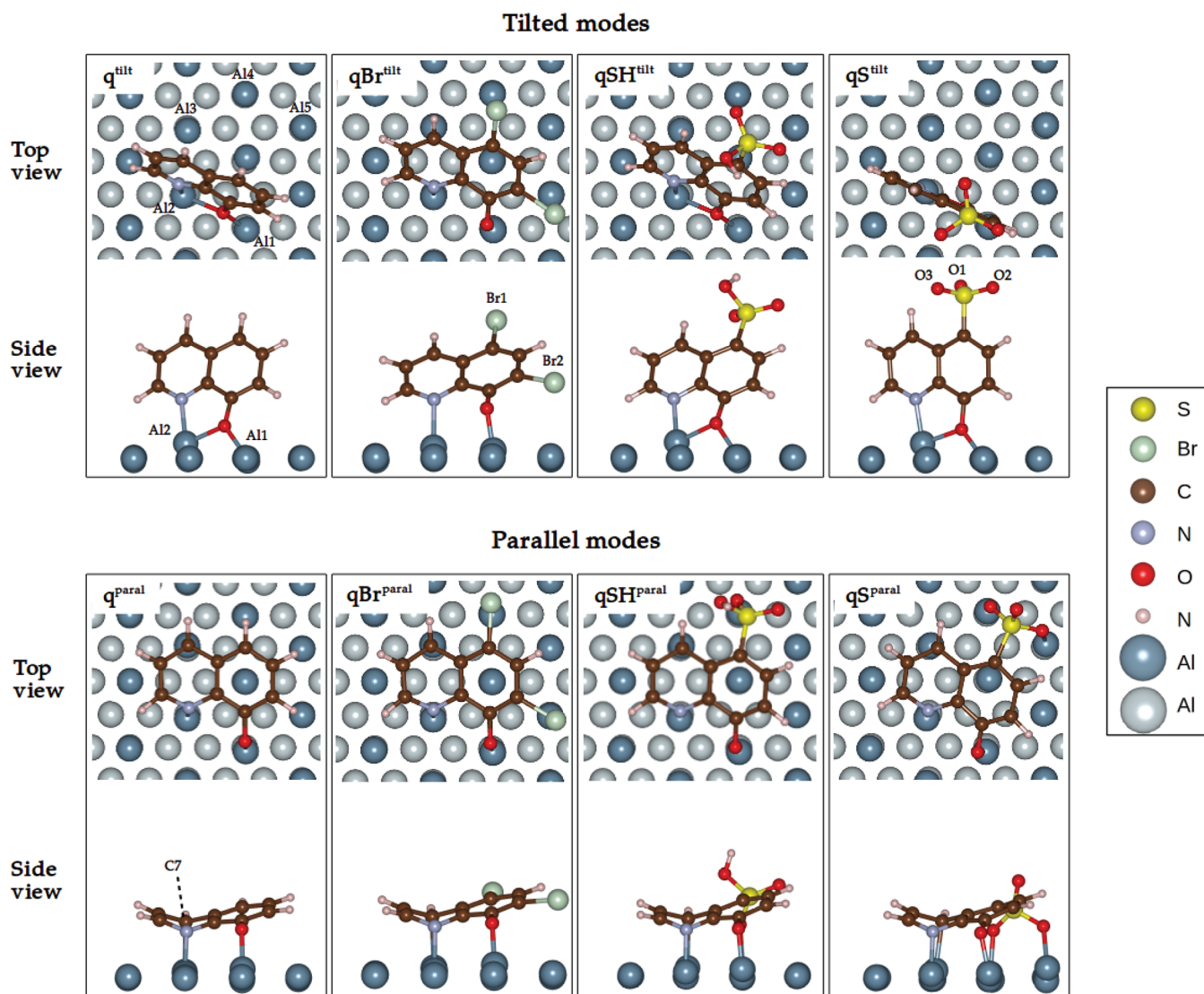


Figure 8. Tilted and parallel adsorption geometries for the q , qBr , qSH , and qS molecules. Dark blue: surface atoms (layer S). Light blue: subsurface atoms (layers S 1 and S 2). PBE D2 level of calculation.

Table 6. Relative Total Energies (the Reference Is the Total Energy of the Tilted Geometry of the q and qX Species), Adsorption Energies, Deformation Energies of the Molecule and of the Slab upon Adsorption, Interaction Energies between the Molecule and the Al(111) Surface and van der Waals Contribution (in eV), and Charge on the Adsorbed Molecule (in e)^b

	q ^{tilt}	q ^{paral}	qBr ^{tilt}	qBr ^{paral}	qSH ^{tilt}	qSH ^{paral}	qS ^{tilt}	qS ^{paral}
ΔE	0	0.11	0	0.16	0	0.21	0	1.82
$E_{\text{ads}}^{\text{mol}}$	3.59 ^a	3.48 ^a	3.51	3.67	3.70	3.91		
$E_{\text{deform}}^{\text{mol}}$	0.54	1.69	0.35	1.84	0.51	2.04		
$E_{\text{deform}}^{\text{slab}}$	0.43	0.27	0.19	0.28	0.42	0.32		
$E_{\text{int}}^{\text{slab/mol}}$	4.57	5.43	4.04	5.78	4.63	6.29		
$E_{\text{int}}^{\text{slab/mol}}(\text{vdW})$	0.66	1.26	0.96	1.50	0.74	1.39		
Q_{mol}	1.15	2.02	1.09	2.13	1.25	2.26	1.69	3.03

^aReference 17. ^bPBE D2 level of calculation.

Table 7. Shortest Distances between Surface Al Atoms and the Atoms of the Molecules (in Å)^a

	q ^{tilt}	q ^{paral}	qBr ^{tilt}	qBr ^{paral}	qSH ^{tilt}	qSH ^{paral}	qS ^{tilt}	qS ^{paral}
$d_{\text{Al1-O}}$	1.909	1.800	1.818	1.809	1.916	1.814	1.892	1.818
$d_{\text{Al2-O}}$	2.034				2.057		1.977	
$d_{\text{Al2-N}}$	2.043	1.916	2.085	1.920	2.038	1.919	2.002	1.909
$d_{\text{Al3-C7}}$		2.192		2.174		2.200		2.202
$d_{\text{Al-O2}}$						2.059		1.930
$d_{\text{Al-O3}}$								1.935

^aPBE D2 level of calculation.

atoms of the molecules and surface Al atoms are given in Table 7. In the case of adsorption on a bridge site of the surface (Figure 3), two bonds are formed, and two bond lengths ($d_{\text{Al1-O}}$ and $d_{\text{Al2-O}}$) are given. For the tilted configurations, the tilt angle can be defined as the angle formed between the C5–C6 bond and its projection on the Al(111) surface. The tilt angle values are 64.9°, 40.6°, 52.1°, and 87.2°, respectively, for the q, qBr, qSH, and qS species. These variations of the tilt angle are due to the intensity of the interactions of the molecules with the Al surface that governs the adsorption geometry.

For the q molecule, the tilted mode is more stable than the parallel mode by 0.11 eV. For this tilted configuration, the adsorption energy is –3.59 eV,¹⁷ showing a strong adsorption of the molecule on the Al(111) surface. The molecule is bound to the surface by the O atom (bridge position on the Al(111) surface, $d_{\text{Al1-O}} = 1.909$ Å and $d_{\text{Al2-O}} = 2.034$ Å) and the N atom (top position, $d_{\text{Al-N}} = 2.043$ Å). This leads to a deformation of the molecule ($E_{\text{deform}}^{\text{mol}} = 0.54$ eV). The slab is also deformed ($E_{\text{def}}^{\text{slab}} = 0.43$ eV) as the Al atom bound to both the O and N atoms is pulled out of the surface ($\Delta z_{\text{Al2}} = 0.652$ Å in Figure 8) upon adsorption. The interaction energy $E_{\text{int}}^{\text{slab/mol}}$ corresponds to the energy associated with both chemical and van der Waals bonding between the molecule and the surface, without taking into account the value of the energy of deformation of the molecules and the slab. The interaction energy of the tilted mode is –4.57 eV. It again shows a strong interaction between the molecule and the Al(111) surface, and 14.4% of the interaction energy comes from van der Waals interactions (–0.66 eV). The adsorption energy of the parallel mode is –3.48 eV,¹⁷ also indicating a strong interaction with the Al(111) surface. In that case, the molecule is strongly distorted upon adsorption with a deformation energy of 1.69 eV. This strong value corresponds to the deformation of the pyridine ring (see Figure 8) as the C7 atom forms a bond with one Al surface atom ($d_{\text{Al3-C7}} = 2.192$ Å) in addition to the bonding of the molecule via the O atom ($d_{\text{Al1-O}} = 1.800$ Å) and the N atom ($d_{\text{Al-N}} = 1.916$ Å) in top positions on the Al(111)

surface. The deformation energy of the slab is of 0.27 eV, showing a weakly deformed slab. The interaction energy $E_{\text{int}}^{\text{slab/mol}}$ of the parallel mode is of –5.43 eV. The binding is thus stronger for the parallel mode than for the tilted mode because of the Al3–C7 bond, as well as by stronger van der Waals interactions (–1.26 eV and 23.2% of the interaction energy) in the parallel mode than in the tilted mode.

The strong interaction between the qX species and the Al(111) surface runs for all the molecules with adsorption energies values from –3.51 eV to –3.91 eV. In contrast to the adsorption of the q molecule, for which the most stable geometry on the Al(111) surface is the tilted one, the parallel adsorption mode is more stable than the tilted mode by 0.16, 0.21, and 1.82 eV for qBr, qSH, and qS, respectively. It is due to a stronger interaction with the surface Al atoms in the parallel mode for the qBr and qSH molecules ($E_{\text{int}}^{\text{slab/mol}} = -5.78$ eV and –6.29 eV) than for the q molecule ($E_{\text{int}}^{\text{slab/mol}} = -5.43$ eV) and high stabilizing van der Waals contribution to the interaction energy (25.9% and 22.1%, respectively). Moreover, the interaction of the Br2 atom on C3 with the Al(111) surface gives rise to a tilted mode less stable for qBr than the parallel geometry. For the qSH species, the adsorption geometry is close to the parallel one for qS, but only one O atom of the SO₃H group is in interaction with atoms of the Al(111) surface ($d_{\text{Al-O2}} = 2.059$ Å). For the qS molecule, the parallel mode is the most stable configuration because the molecule is chemisorbed on the surface by the O atom ($d_{\text{Al1-O}} = 1.818$ Å), the N atom ($d_{\text{Al1-N}} = 1.909$ Å), and the C7 atom ($d_{\text{Al3-C7}} = 2.202$ Å) like for the parallel mode of the other qX molecules, as well as by two oxygen atoms of the SO₃ group ($d_{\text{Al-O2}} = 1.930$ Å and $d_{\text{Al-O3}} = 1.935$ Å). For the qS molecule, one conformation with the molecule adsorbed on the surface by the SO₃ group was also determined and is presented in Table S4.

The deformation energies of the slab and the molecules do not change drastically upon the series of inhibitors for the tilted mode. For the parallel mode, the deformation energy of the qSH molecule is stronger because of the additional

bonding between the surface Al atoms and the sulfonic group. Thanks to its adsorption geometry, the **qS** species might have a similar high value for the deformation energy upon adsorption. The bond lengths in the molecules, in their free state and for the parallel adsorption mode (strongest deformations of the molecules upon adsorption), are presented in Table S5. The bond lengths are modified in the molecules upon adsorption on Al(111) showing a strong electronic reorganization. In the free **q**, **qBr**, and **qSH** species, the C–C bond length values in the pyridine ring range from 1.384 to 1.433 Å, and the C–N bond length values range from 1.332 to 1.344 Å. All these values are in favor of an aromatic character in the pyridine ring.⁷⁸ In the phenol ring, the C1–C2, C2–C3, C5–C6, and C6–C1 bond lengths show also electron delocalization on these C–C bonds, whereas the C3–C4 and C4–C5 bonds are larger (1.454–1.499 Å). The C–O distance is 1.239–1.249 Å, and it is characteristic of a phenoxy radical bond.⁷⁹ In the adsorbed species (parallel adsorption mode), the aromatic character of the phenol ring and the pyridine ring is modified. The phenol ring of the molecules is not very distorted and shows a more aromatic character (C–C distances between 1.384 and 1.426 Å; C–O distances between 1.335 and 1.346 Å, showing single bonds with a partial double bond character⁸⁰) than in the free state. The pyridine ring is strongly distorted, and the aromatic character is strongly lowered in the cycle. The C6–C7 and C7–C8 distances could show a single bond between one Csp² and one Csp³ atoms.⁸¹ The C8–C9 bond length of 1.36 Å is in favor of a double bond. The C5–N and C9–N bonds are enlarged with bond lengths closer to single bonds with a partial double bond character.

In the periodic DFT approach, the type and the strength of the interactions between an adsorbate and a substrate are usually characterized by the evaluation of the electron transfer upon adsorption (Table 6) and the plotting of the electron density at the adsorbate/substrate interface (Figure 9). For the **q** species, the QTAIM charges calculated before and after adsorption show that the adsorbed molecules are negatively charged with a higher charge (in absolute value) for the parallel mode (–2.02 e) than for the tilted mode (–1.15 e). The charges are even bigger for the **qX** molecules, with charges ranging from –1.09 to –1.69 e for the tilted mode and –2.13 e to –3.03 e for the parallel geometry. These large values of the charges on the adsorbed species already suggest an ionic character of the bonds between anionic molecules and slightly cationic Al surface atoms. The electron density ρ presented in Figure 9 for the **q** and **qS** species on Al(111) could evidence also, by the presence of electrons at the molecule/metal interface, some covalent bonding between the N and O atoms and surface Al atoms (tilted adsorption mode), with in addition bonds between C atoms and surface Al atoms in the parallel geometry. For the **qS** species specially, the covalent bonding of the SO₃ group with surface Al atoms could also exist for the parallel adsorption mode. However, as stated by Gillespie,⁸² “there are no purely ionic bonds even in crystals, since the ions are not truly spherical and there is always a small amount of density shared between the atoms”. A further investigation of the bonding at the molecule/metal interface was then performed using QTAIM descriptors to quantify the ionic and covalent nature of the interactions, and it is described below.

3.2.2. *Topological Analyses of the Charge Density of the q/Al(111) and qX/Al(111) Systems.* Selected values of the

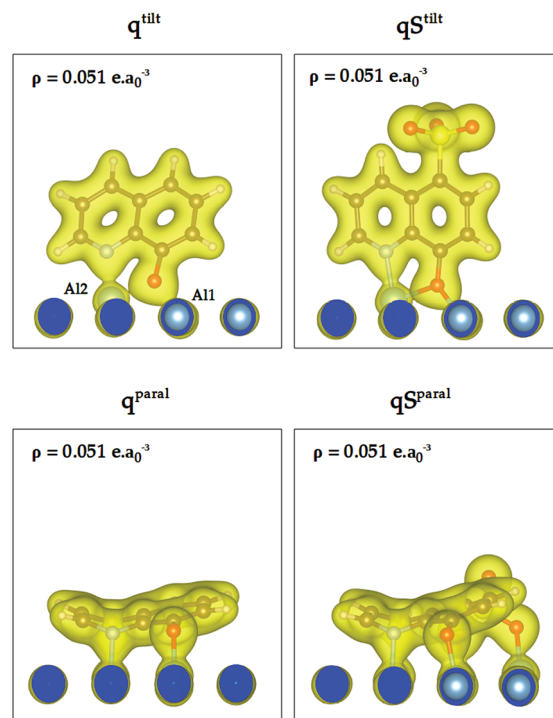


Figure 9. Electron density ρ for the **q/Al(111)** and **qS/Al(111)** systems. a_0 is the Bohr radius.

electron density ρ and Laplacian of the electron density $\nabla^2\rho$ at Al–O and Al–N bond critical points (BCPs) are presented in Table 8 and Tables S6 and S7, together with $\frac{|V_{\text{bcp}}|}{G_{\text{bcp}}}$ and $\frac{H_{\text{bcp}}}{\rho_{\text{bcp}}}$ values. The values of the selected QTAIM descriptors are very similar over the series. At all BCPs, the electron density ρ_{bcp} values in Table 8 are weak in a range from 0.05 to 0.09 e. This suggests van der Waals interactions or ionic bonding between the molecules and the Al(111) surface. This is consistent with the large charges on the species observed and the strong contribution of dispersive forces to the interaction energy between the molecules and the aluminum surface. Large positive Laplacian of the electron density values is observed also in favor of ionic bonding. The QTAIM descriptors $\frac{|V_{\text{bcp}}|}{G_{\text{bcp}}}$ and $\frac{H_{\text{bcp}}}{\rho_{\text{bcp}}}$ of Al–O and Al–N bond critical points (BCPs) are also very similar all over the series of **qX/Al(111)** systems. The $\frac{|V_{\text{bcp}}|}{G_{\text{bcp}}}$ values slightly larger than 1 (except for **q^{tilt}** with a value of 0.985 for the Al2–O bond) point again toward the ionic bonding domain at the borderline with the intermediate bonding regime including dative bonding. Small negative energy densities suggest however a very weak covalence degree as indicated by the $\frac{H_{\text{bcp}}}{\rho_{\text{bcp}}}$ values. For the parallel adsorption geometries, the C7 atom of the molecules is also bound to the surface Al atom, and the values of the QTAIM descriptors in Table 8 account also for an ionic bonding with a small covalence degree.

4. CONCLUSION

In this work, we investigated the influence of the substitution of H atoms by Br atoms and the SO₃[–] group on the reactivity of hydroxyquinoline species toward aluminum. We thus

Table 8. Relevant QTAIM Descriptors (in au^a) Related to the Al–O, Al–N, and Al–C7 Bonds in the q/Al(111) and qX/Al(111) Systems^b

	q^{tilt}	q^{paral}	qBr^{tilt}	qBr^{paral}	qSH^{tilt}	qSH^{paral}	qS^{tilt}	qS^{paral}
BCP Al1 O								
ρ_{bcp}	0.066	0.089	0.082	0.086	0.065	0.085	0.070	0.086
$\nabla^2\rho$	0.336	0.526	0.530	0.550	0.327	0.533	0.353	0.537
$\frac{ V_{\text{bcp}} }{G_{\text{bcp}}}$	1.032	1.050	1.001	1.019	1.034	1.020	1.050	1.022
$\frac{H_{\text{bcp}}}{\rho_{\text{bcp}}}$	0.043	0.078	0.002	0.031	0.044	0.033	0.066	0.035
BCP Al2 O								
ρ_{bcp}	0.051				0.049		0.058	
$\nabla^2\rho$	0.253				0.213		0.295	
$\frac{ V_{\text{bcp}} }{G_{\text{bcp}}}$	0.985				1.016		1.007	
$\frac{H_{\text{bcp}}}{\rho_{\text{bcp}}}$	0.018				0.017		0.009	
BCP Al2 N								
ρ_{bcp}	0.060	0.079	0.055	0.078	0.061	0.078	0.067	0.080
$\nabla^2\rho$	0.256	0.377	0.205	0.373	0.248	0.381	0.270	0.391
$\frac{ V_{\text{bcp}} }{G_{\text{bcp}}}$	1.073	1.097	1.097	1.094	1.093	1.088	1.118	1.092
$\frac{H_{\text{bcp}}}{\rho_{\text{bcp}}}$	0.074	0.128	0.100	0.124	0.075	0.117	0.135	0.125
BCP Al3 C7								
ρ_{bcp}		0.057		0.058		0.056		0.055
$\nabla^2\rho$		0.111		0.129		0.116		0.100
$\frac{ V_{\text{bcp}} }{G_{\text{bcp}}}$		1.345		1.309		1.318		1.370
$\frac{H_{\text{bcp}}}{\rho_{\text{bcp}}}$		0.259		0.248		0.243		0.266

^a ρ_{bcp} in e/bohr³, V_{bcp} , G_{bcp} , and H_{bcp} in hartree/bohr³. ^bPBE D2 level of calculation.

compared on the one hand the chelating properties of q^- , qBr^- , qSH^- , and qS^2 anions toward Al^{3+} cations, and on the other hand the adsorption properties of q , qBr , qSH , and qS species on an Al(111) surface.

Formation energies of Alq_3 and $Al(qX)_3$ complexes, with a value of -24.30 ± 0.29 eV in water, show a strong bonding affinity of q^- and qX^{n-} ($n = 1$ or 2) species to the aluminum cations. The small variation of the formation energies in water within the series of complexes evidence that the substitutions on the hydroxyquinoline species do not influence the coordinating properties of these molecules with aluminum cations for the formation of chelates. ELF and QTAIM topological analyses of these complexes showed that the bonding of the deprotonated molecules, i.e., q^- , qBr^- , qSH^- , and qS^2 species, with the Al^{3+} ion is ionic with a very weak covalence degree. The substitution of H atoms on the hydroxyquinoline species only modifies locally the electronic structures of the species, and it is consistent with the small variation of the formation energies of the complexes. It shows that all these chemically modified Hq species could be used without distinction in various applications where stable Al complexes are needed. Other properties of the $Al(qX)$ complexes, i.e., their solubility in water that may be influenced

by the chemical modifications on X1 and X2 positions, have to be studied. This will be the aim of further investigations.

Periodic calculations on the adsorption of qX species on an Al(111) surface give rise to different most stable geometries for the q and the modified qX species, i.e., qBr , qSH , and qS . All the species are strongly in interaction with the Al(111) surface, with values of the adsorption energy of -3.69 ± 0.21 eV for the most stable geometries. Thus the chemical modifications on the hydroxyquinoline molecule influence only slightly the adsorption energies. It was also shown that the different adsorption modes are driven by O, N and additional interactions of the substituents with the Al surface. The latter interactions modify the adsorption geometries of the species on Al(111). These different adsorption modes could lead to q and qX layers of different compacity, with thus different protecting efficiency, in particular against corrosion. Such studies are in progress combining in vacuum and in solvent computations.

The ELF and QTAIM descriptors of both models studied in this work are indicative of ionic bonding with a weak covalence degree, between the deprotonated Hq and HqX species and either the aluminum cation or the aluminum surface. The species are thus held together by the Coulombic interactions between the adsorbed species that are negatively charged and

the polarized, cationic like, aluminum surface. This is consistent with the plots of the electron density showing several regions of shared electron density at the interface between the O, N and several C or H atoms of the adsorbed molecule and the Al surface atoms, suggesting a weak covalent character. The latter graphical qualitative electron density analysis was here however refined with the quantitative descriptors of the topological analyses.

■ ASSOCIATED CONTENT

● Supporting Information

The Supporting Information is available free of charge at <https://pubs.acs.org/doi/10.1021/acs.inorgchem.0c01972>.

Table S1: population of ELF basins (in e) for free q^- and qX^{n-} anions and for Alq_3 and $Al(qX)_3$ complexes (for latter systems, descriptors are averaged over three equivalent bonds); Table S2: QTAIM charges (in e) for free q^- and qX^{n-} anions and for Alq_3 and $Al(qX)_3$ complexes (for latter systems, charges are averaged over three equivalent atoms); Table S3: complex formation energy $E_{form}^{complex}$ in vacuum (in eV); Table S4: relative total energies (reference is total energy of tilted geometry for q and qX species), adsorption energies, deformation energies of molecule and of slab upon adsorption, interaction energies between molecule and Al(111) surface and van der Waals contribution (in eV), charge on adsorbed molecule (in e); Table S5: bond lengths (in Å) for free qX and qX species adsorbed on Al(111) in parallel adsorption mode ($qX^{p=al}$); Table S6: QTAIM descriptors (in au) related to Al–C5, A–C9, Al–C3, Al–Br1, and Al–Br2 bonds between atoms of q and qX molecules and surface Al atoms in $q/Al(111)$ and $qX/Al(111)$ systems; and Table S7: QTAIM descriptors (in au) related to Al–H(C9) and A–H(C3) bonds between atoms of q and qX molecules and surface Al atoms in $q/Al(111)$ and $qX/Al(111)$ systems (PDF)

■ AUTHOR INFORMATION

Corresponding Author

Corinne Lacaze Dufaure – CIRIMAT, Université de Toulouse, CNRS, 31030 Toulouse, France; orcid.org/0000-0003-3151-2685; Email: corinne.dufaure@ensiacet.fr

Authors

Yann Bulteau – CIRIMAT, Université de Toulouse, CNRS, 31030 Toulouse, France

Christine Lepetit – LCC CNRS, Université de Toulouse, CNRS, UPS, F 31077 Toulouse, France; orcid.org/0000-0002-0008-9506

Complete contact information is available at: <https://pubs.acs.org/doi/10.1021/acs.inorgchem.0c01972>

Notes

The authors declare no competing financial interest.

■ ACKNOWLEDGMENTS

This work was granted access to the HPC resources of CALMIP supercomputing center under the allocation 2019 [p12174]. It was also supported by the French Ministry of Higher Education and Research [Y.B., PhD grant]. C.L. D.

would like to acknowledge N. Tarrat (CEMES, Toulouse) for helpful suggestions.

■ REFERENCES

- (1) Albrecht, M.; Fiege, M.; Osetka, O. 8 Hydroxyquinolines in metallosupramolecular chemistry. *Coord. Chem. Rev.* 2008, 252, 812–824.
- (2) Barros, F. C. F.; Sousa, F. W.; Cavalcante, R. M.; Carvalho, T. V.; Dias, F. S.; Queiroz, D. C.; Vasconcelos, L. C. G.; Nascimento, R. F. Removal of Copper, Nickel and Zinc Ions from Aqueous Solution by Chitosan 8 Hydroxyquinoline Beads. *Clean: Soil, Air, Water* 2008, 36, 292–298.
- (3) Ramos, M. L.; Justino, L. L. G.; Salvador, A. I. N.; de Sousa, A. R. E.; Abreu, P. E.; Fonseca, S. M.; Burrows, H. D. NMR, DFT and luminescence studies of the complexation of Al(III) with 8 hydroxyquinoline 5 sulfonate. *Dalton Trans.* 2012, 41, 12478–12489.
- (4) Tang, C. W.; VanSlyke, S. A. Organic electroluminescent diodes. *Appl. Phys. Lett.* 1987, 51, 913–915.
- (5) Shen, Z.; Burrows, P. E.; Bulović, V.; Forrest, S. R.; Thompson, M. E. Three Color, Tunable, Organic Light Emitting Devices. *Science* 1997, 276, 2009–2011.
- (6) Prachayasittikul, V.; Prachayasittikul, S.; Ruchirawat, S.; Prachayasittikul, V. 8 Hydroxyquinolines: a review of their metal chelating properties and medicinal applications. *Drug Des., Dev. Ther.* 2013, 7, 1157–1178.
- (7) Garrigues, L.; Pèbère, N.; Dabosi, F. An investigation of the corrosion inhibition of pure aluminum in neutral and acidic chloride solutions. *Electrochim. Acta* 1996, 41, 1209–1215.
- (8) Lamaka, S.; Zheludkevich, M.; Yasakau, K.; Montemor, M.; Ferreira, M. High effective organic corrosion inhibitors for 2024 aluminium alloy. *Electrochim. Acta* 2007, 52, 7231–7247.
- (9) Marcelin, S.; Pèbère, N. Synergistic effect between 8 hydroxyquinoline and benzotriazole for the corrosion protection of 2024 aluminium alloy: A local electrochemical impedance approach. *Corros. Sci.* 2015, 101, 66–74.
- (10) Soliman, H. Influence of 8 hydroxyquinoline addition on the corrosion behavior of commercial Al and Al HO411 alloys in NaOH aqueous media. *Corros. Sci.* 2011, 53, 2994–3006.
- (11) Verma, C.; Quraishi, M.; Ebenso, E. Quinoline and its derivatives as corrosion inhibitors: A review. *Surf. Interfaces* 2020, 21, 100634–100646.
- (12) Fairman, B.; Medel, A. S. Improved Determination of Aluminium Species in Waters Using FIA Separation/Fluorimetric Detection Techniques. *Int. J. Environ. Anal. Chem.* 1993, 50, 161–171.
- (13) Li, S. M.; Zhang, H. R.; Liu, J. H. Corrosion behavior of aluminum alloy 2024 T3 by 8 hydroxy quinoline and its derivative in 3.5% chloride solution. *Trans. Nonferrous Met. Soc. China* 2007, 17, 318–325.
- (14) Costa, D.; Marcus, P. *Molecular Modeling of Corrosion Processes: Scientific Development and Engineering Applications*; John Wiley and Sons, Inc.: Hoboken, 2015; Chapter 5, DOI: 10.1002/9781119057666.
- (15) Chiter, F.; Lacaze Dufaure, C.; Tang, H.; Pèbère, N. DFT Studies of the Bonding Mechanism of 8 Hydroxyquinoline and Derivatives on the (111) Aluminum Surface. *Phys. Chem. Chem. Phys.* 2015, 17, 22243–22258.
- (16) Chiter, F.; Bonnet, M. L.; Lacaze Dufaure, C.; Tang, H.; Pèbère, N. Corrosion protection of Al(111) by 8 hydroxyquinoline: a comprehensive DFT study. *Phys. Chem. Chem. Phys.* 2018, 20, 21474–21486.
- (17) Bulteau, Y.; Tarrat, N.; Pèbère, N.; Lacaze Dufaure, C. 8 Hydroxyquinoline complexes (Alq_3) on Al(111): atomic scale structure, energetics and charge distribution. *New J. Chem.* 2020, 44, 15209–15222.
- (18) Obot, I.; Macdonald, D.; Gasem, Z. Density Functional Theory (DFT) as a powerful tool for designing new organic corrosion inhibitors. Part 1: An overview. *Corros. Sci.* 2015, 99, 1–30.

- (19) Taylor, C. D.; Chandra, A.; Vera, J.; Sridhar, N. A Multiphysics Perspective on Mechanistic Models for Chemical Corrosion Inhibitor Performance. *J. Electrochem. Soc.* **2015**, *162*, C369–C375.
- (20) Bader, R. F. W. *Atoms In Molecules*; Clarendon Press: 1990.
- (21) Bianchi, R.; Gervasio, G.; Marabello, D. Experimental Electron Density Analysis of Mn₂(CO)₁₀: Metal–Metal and Metal–Ligand Bond Characterization. *Inorg. Chem.* **2000**, *39*, 2360–2366.
- (22) Cortes Guzman, F.; Bader, R. Complementarity of QTAIM and MO theory in the study of bonding in donor–acceptor complexes. *Coord. Chem. Rev.* **2005**, *249*, 633–662.
- (23) Boukallaba, M.; Kerkeni, B.; Lepetit, C.; Berthomieu, D. Coordination complexes of 4 methylimidazole with ZnII and CuII in gas phase and in water: a DFT study. *J. Mol. Model.* **2016**, *22*, 301–312.
- (24) Lepetit, C.; Fau, P.; Fajerweg, K.; Kahn, M. L.; Silvi, B. Topological analysis of the metal metal bond: a tutorial review. *Coord. Chem. Rev.* **2017**, *345*, 150–181.
- (25) Lepetit, C.; Vabre, B.; Canac, Y.; Alikhani, M.; Zargarian, D. Pentacoordinated, square pyramidal cationic PCP Ni(II) pincer complexes: ELF and QTAIM topological analyses of nickel triflate interactions. *Theor. Chem. Acc.* **2018**, *137*, 141–163.
- (26) Aray, Y.; Rodriguez, J.; Vega, D. Topology of the Electron Density and Cohesive Energy of the Face Centered Cubic Transition Metals. *J. Phys. Chem. B* **2000**, *104*, 4608–4612.
- (27) Vega, D.; Almeida, D. AIM UC: An application for QTAIM analysis. *J. Comput. Methods Sci. Eng.* **2014**, *14*, 131–136.
- (28) Aray, Y.; Barrios, A. D. Exploring the electron density localization in MoS₂ nanoparticles using a localized electron detector: Unraveling the origin of the onedimensional metallic sites on MoS₂ catalysts. *Phys. Chem. Chem. Phys.* **2018**, *20*, 20417–20426.
- (29) Becke, A. D.; Edgecombe, K. E. A simple measure of electron localization in atomic and molecular systems. *J. Chem. Phys.* **1990**, *92*, 5397–5403.
- (30) Silvi, B.; Savin, A. Classification of chemical bonds based on topological analysis of electron localization function. *Nature* **1994**, *371*, 683–686.
- (31) Lepetit, C.; Silvi, B.; Chauvin, R. ELF Analysis of Out of Plane Aromaticity and In Plane Homoaromaticity in Carbo[N]annulenes and [N]Pericyclines. *J. Phys. Chem. A* **2003**, *107*, 464–473.
- (32) Savin, A.; Nesper, R.; Wengert, S.; Fässler, T. F. ELF: The Electron Localization Function. *Angew. Chem., Int. Ed. Engl.* **1997**, *36*, 1808–1832.
- (33) Loffreda, D. Structural Identification of Conjugated Molecules on Metal Surfaces by Means of Soft Vibrations. *Angew. Chem., Int. Ed.* **2006**, *45*, 6537–6540.
- (34) Le Bahers, T.; Adamo, C.; Ciofini, I. Theoretical determination of the pK_as of the 8 hydroxyquinoline 5 sulfonic acid: A DFT based approach. *Chem. Phys. Lett.* **2009**, *472*, 30–34.
- (35) Frisch, M. J. et al. *Gaussian 09*, Revision D.01; Gaussian, Inc.: Wallingford, CT, 2016.
- (36) Perdew, J. P.; Burke, K.; Ernzerhof, M. Generalized Gradient Approximation Made Simple. *Phys. Rev. Lett.* **1996**, *77*, 3865–3868.
- (37) Weigend, F.; Ahlrichs, R. Balanced basis sets of split valence, triple zeta valence and quadruple zeta valence quality for H to Rn: Design and assessment of accuracy. *Phys. Chem. Chem. Phys.* **2005**, *7*, 3297–3305.
- (38) Weigend, F. Accurate Coulomb fitting basis sets for H to Rn. *Phys. Chem. Chem. Phys.* **2006**, *8*, 1057–1065.
- (39) Grimme, S. Semiempirical GGA type density functional constructed with a long range dispersion correction. *J. Comput. Chem.* **2006**, *27*, 1787–1799.
- (40) Grimme, S.; Antony, J.; Ehrlich, S.; Krieg, H. A consistent and accurate ab initio parametrization of density functional dispersion correction (DFT D) for the 94 elements H Pu. *J. Chem. Phys.* **2010**, *132*, 154104–154111.
- (41) Macchi, P.; Proserpio, D.; Sironi, A. Experimental Electron Density in a Transition Metal Dimer: Metal Metal and Metal Ligand Bonds. *J. Am. Chem. Soc.* **1998**, *120*, 13429–13435.
- (42) Espinosa, E.; Alkorta, I.; Elguero, J.; Molins, E. From weak to strong interactions: A comprehensive analysis of the topological and energetic properties of the electron density distribution involving X HF Y systems. *J. Chem. Phys.* **2002**, *117*, 5529–5542.
- (43) Poater, J.; Duran, M.; Sola, M.; Silvi, B. Theoretical Evaluation of Electron Delocalization in Aromatic Molecules by Means of Atoms in Molecules (AIM) and Electron Localization Function (ELF) Topological Approaches. *Chem. Rev.* **2005**, *105*, 3911–3947.
- (44) Silvi, B.; Gillespie, R. J.; Gatti, C. Electron density analysis. *Comprehensive Inorganic Chemistry II* **2013**, *9*, 187–226.
- (45) Silvi, B. How topological partitions of the electron distributions reveal delocalization. *Phys. Chem. Chem. Phys.* **2004**, *6*, 256–260.
- (46) Noury, S.; Krokidis, X.; Fuster, F.; Silvi, B. Computational tools for the electron localization function topological analysis. *Comput. Chem.* **1999**, *23*, 597–604.
- (47) CSCS, Molekel. <https://www.cscs.ch/molkel/> (accessed 2020 11 23).
- (48) Bader, R. F. W.; Essen, H. The characterization of atomic interactions. *J. Chem. Phys.* **1984**, *80*, 1943–1960.
- (49) Keith, T. A. *AIMALL 1997*; TK Gristmill Software: Overland Park KS, USA, 2019. <https://aim.tkgristmill.com> (accessed 2020 11 23).
- (50) Kokalj, A.; Peljhan, S.; Finšgar, M.; Milošev, I. What Determines the Inhibition Effectiveness of ATA, BTAH, and BTAOH Corrosion Inhibitors on Copper? *J. Am. Chem. Soc.* **2010**, *132*, 16657–16668.
- (51) Kokalj, A.; Peljhan, S.; Koller, J. The Effect of Surface Geometry of Copper on Dehydrogenation of Benzotriazole. Part II. *J. Phys. Chem. C* **2014**, *118*, 944–954.
- (52) Poberžnik, M.; Costa, D.; Hemeryck, A.; Kokalj, A. Insight into the Bonding of Silanols to Oxidized Aluminum Surfaces. *J. Phys. Chem. C* **2018**, *122*, 9417–9431.
- (53) Kresse, G.; Hafner, J. Ab initio molecular dynamics for liquid metals. *Phys. Rev. B: Condens. Matter Mater. Phys.* **1993**, *47*, 558–561.
- (54) Kresse, G.; Furthmüller, J. Efficient iterative schemes for ab initio total energy calculations using a plane wave basis set. *Phys. Rev. B: Condens. Matter Mater. Phys.* **1996**, *54*, 11169–11186.
- (55) Kresse, G.; Furthmüller, J. Efficiency of ab initio total energy calculations for metals and semiconductors using a plane wave basis set. *Comput. Mater. Sci.* **1996**, *6*, 15–50.
- (56) Blöchl, P. E. Projector augmented wave method. *Phys. Rev. B: Condens. Matter Mater. Phys.* **1994**, *50*, 17953–17979.
- (57) Kresse, G.; Joubert, D. From ultrasoft pseudopotentials to the projector augmented wave method. *Phys. Rev. B: Condens. Matter Mater. Phys.* **1999**, *59*, 1758–1775.
- (58) Perdew, J. P.; Burke, K.; Ernzerhof, M. Generalized Gradient Approximation Made Simple [Phys. Rev. Lett. 77, 3865 (1996)]. *Phys. Rev. Lett.* **1997**, *78*, 1396–1396.
- (59) Schiavo, E.; Munoz Garcia, A.; Barone, V.; Vittadini, A.; Casarin, M.; Forrer, D.; Pavone, M. Tuning dispersion correction in DFT D2 for metal molecule interactions: A tailored reparameterization strategy for the adsorption of aromatic systems on Ag(111). *Chem. Phys. Lett.* **2018**, *693*, 28–33.
- (60) Methfessel, M.; Paxton, A. T. High precision sampling for Brillouin zone integration in metals. *Phys. Rev. B: Condens. Matter Mater. Phys.* **1989**, *40*, 3616–3621.
- (61) Monkhorst, H. J.; Pack, J. D. Special points for Brillouin zone integrations. *Phys. Rev. B* **1976**, *13*, 5188–5192.
- (62) Neugebauer, J.; Scheffler, M. Adsorbate substrate and adsorbate adsorbate interactions of Na and K adlayers on Al(111). *Phys. Rev. B: Condens. Matter Mater. Phys.* **1992**, *46*, 16067–16080.
- (63) Tyson, W. R.; Miller, W. Surface free energies of solid metals: Estimation from liquid surface tension measurements. *Surf. Sci.* **1977**, *62*, 267–276.
- (64) Momma, K.; Izumi, F. VESTA: a three dimensional visualization system for electronic and structural analysis. *J. Appl. Crystallogr.* **2008**, *41*, 653–658.

- (65) Momma, K.; Izumi, F. VESTA 3 for three dimensional visualization of crystal, volumetric and morphology data. *J. Appl. Crystallogr.* **2011**, *44*, 1272–1276.
- (66) Tang, W.; Sanville, E.; Henkelman, G. A grid based Bader analysis algorithm without lattice bias. *J. Phys.: Condens. Matter* **2009**, *21*, 084204.
- (67) Abramov, Y. A. On the Possibility of Kinetic Energy Density Evaluation from the Experimental Electron Density Distribution. *Acta Crystallogr., Sect. A: Found. Crystallogr.* **1997**, *A53*, 264–272.
- (68) Fuster, F.; Sevin, A.; Silvi, B. Topological analysis of the electron localization function (ELF) applied to the electrophilic aromatic substitution. *J. Phys. Chem. A* **2000**, *104*, 852–858.
- (69) Fuster, F.; Grabowski, S. J. Intramolecular Hydrogen Bonds: the QTAIM and ELF Characteristics. *J. Phys. Chem. A* **2011**, *115*, 10078–10086.
- (70) Murgich, J.; Franco, H. J. A Density Functional Theory Study of the Topology of the Charge Density of Complexes of 8 Hydroxyquinoline with Mn (III), Fe (III), and Co (III). *J. Phys. Chem. A* **2009**, *113*, S205–S211.
- (71) Curioni, A.; Boero, M.; Andreoni, W. Alq₃: ab initio calculations of its structural and electronic properties in neutral and charged states. *Chem. Phys. Lett.* **1998**, *294*, 263–271.
- (72) Wang, Y. P.; Han, X. F.; Wu, Y. N.; Cheng, H. P. Adsorption of tris(8 hydroxyquinoline)aluminum molecules on cobalt surfaces. *Phys. Rev. B: Condens. Matter Mater. Phys.* **2012**, *85*, 144430–144440.
- (73) Yanagisawa, S.; Lee, K.; Morikawa, Y. First principles theoretical study of Alq(3)/Al interfaces: Origin of the interfacial dipole. *J. Chem. Phys.* **2008**, *128*, 244704–244717.
- (74) Halls, M. D.; Schlegel, H. B. Molecular Orbital Study of the First Excited State of the OLED Material Tris(8 hydroxyquinoline) aluminum(III). *Chem. Mater.* **2001**, *13*, 2632–2640.
- (75) Cölle, M.; Dinnebier, R. E.; Brütting, W. The structure of the blue luminescent delta phase of tris(8 hydroxyquinoline)aluminium (iii) (Alq₃). *Chem. Commun.* **2002**, 2908–2909.
- (76) Marenich, A. V.; Cramer, C. J.; Truhlar, D. G. Universal Solvation Model Based on Solute Electron Density and on a Continuum Model of the Solvent Defined by the Bulk Dielectric Constant and Atomic Surface Tensions. *J. Phys. Chem. B* **2009**, *113*, 6378–6396.
- (77) Hansch, C.; Leo, A.; Taft, R. W. A Survey of Hammett Substituent Constants and Resonance and Field Parameters. *Chem. Rev.* **1991**, *91*, 165–195.
- (78) *Handbook of Chemistry and Physics*, 63rd ed.; CRC Press: 1984.
- (79) Computational Chemistry Comparison & Benchmark Data Base, version 21; August 2020. <https://www.cccbdb.nist.gov/> (accessed 2020 11 23).
- (80) Demaison, J.; Császár, A. Equilibrium CO bond lengths. *J. Mol. Struct.* **2012**, *1023*, 7–14.
- (81) Fox, M.; Whitesell, J. *Organische Chemie: Grundlagen Mechanismen, Bioorganische Anwendungen*; Spektrum Akademischer Verlag: 1995.
- (82) Gillespie, R. Electron Densities, Atomic Charges, and Ionic, Covalent, and Polar Bonds. *J. Chem. Educ.* **2001**, *78*, 1688–1691.

Supporting Information

Selective Coordination of Self-Assembled Hexanuclear [Ni₄Ln₂] and [Ni₂Mn₂Ln₂] (Ln = Dy^{III}, Tb^{III} and Ho^{III}) Complexes: Stepwise Synthesis, Structures and Magnetic Properties

Avik Bhanja,^a Michael Schulze,^b Radovan Herchel^c Eufemio Moreno–Pineda^{d,e}, Wolfgang Wernsdorfer^{b,d,f}, Debashis Ray*^a

^a Department of Chemistry, Indian Institute of Technology, Kharagpur 721302, India

^b Physikalisches Institut, Karlsruhe Institute of Technology, D-76131 Karlsruhe, Germany.

^c Department of Inorganic Chemistry, Faculty of Science, Palacky University, 17. listopadu 12, CZ-771 46 Olomouc, Czech Republic

^d Institute of Nanotechnology (INT), Karlsruhe Institute of Technology (KIT), Hermann-von-Helmholtz-Platz 1, D-76344 Eggenstein-Leopoldshafen, Germany.

^e Depto. de Química-Física, Escuela de Química, Facultad de Ciencias Naturales, Exactas y Tecnología, Universidad de Panamá, Panamá, Panamá.

^f CNRS, Institut Néel, F-38042 Grenoble, France.

*E-mail: dray@chem.iitkgp.ac.in

Contents

Table S1	Summary of Crystallographic parameters for complexes 1–6	S3–4
Chart 1	Metal ion binding mode of ligand H ₂ L	S5
Table S2-S4	Continuous Shape Measures calculations for Ni ^{II} , Mn ^{III} and Ln ^{III}	S5–S6
Table S5	BVS calculation for the Mn metal ion	S6
Figure S1	¹ H NMR spectrum of H ₂ L	S6
Figure S2	FT-IR spectra of H ₂ L, complex 1 and complex 4	S6
Figure S3-S4	PXRD pattern of complexes 1–6	S7
Figure S5	Asymmetric unit and core structure of complex 1	S7
Figure S6	Packing diagram of complex 1	S8
Table S6-S7	Bond distances and bond angles of complex 1	S8–10
Figure S7	Molecular structure of complex 2	S10
Table S8-S9	Bond distances and bond angles of complex 2	S10–12
Figure S8	Molecular structure of complex 3	S12
Table S10-S11	Bond distances and bond angles of complex 3	S12–14
Figure S9	Packing diagram of complex 4	S14
Figure S10	Asymmetric unit and core structure of complex 4	S14
Table S12-S13	Bond distances and bond angles of complex 4	S15–16
Figure S11	Molecular structure of complex 6	S16
Table S14-S15	Bond distances and bond angles of complex 6	S17–18
Figure S12	Magnetization vs. Field data for all complexes	S19
Figure S13	AC susceptibility study for complexes 2, 3, 5 and 6	S20
Figure S14	Field dependent AC magnetic susceptibility data of 1 and 4	S20
Figure S15-S16	Cole-Cole plots and Experimental χ' plot of complex 1 and 4	S21
Figure S17	Hysteresis loops for complex 1 and 4	S22
Figure S18	Easy-axes of the ground state for Dy atoms of 1 and 4	S22
Figure S19	DFT calculated spin densities of BS states in 1 and 4	S23
Figure S20	The fit of magnetic susceptibility of 1 with Poly_Aniso	S23
Figure S21	The fit of magnetic susceptibility of 4 with Poly_Aniso	S24

Table S1 Crystallographic data and structure refinement details of **1–6**

Parameters	1	2	3
Formula	C ₇₀ H ₈₆ Dy ₂ N ₄ Ni ₄ O ₂₆	C ₆₆ H ₇₈ Tb ₂ N ₄ Ni ₄ O ₂₆	C ₇₀ H ₈₆ Ho ₂ N ₄ Ni ₄ O ₂₆
F.W.(g mol ⁻¹)	1959.26	1895.96	1964.12
crystal system	triclinic	triclinic	triclinic
space group	P $\bar{1}$	P $\bar{1}$	P $\bar{1}$
Crystal color	Green	Green	Green
Crystal size/mm ³	0.24×0.16×0.12	0.22×0.14×0.12	0.23×0.16×0.10
a/ Å	12.612(5)	12.094(4)	12.6388(17)
b/ Å	12.720(3)	12.689(4)	12.8502(16)
c/ Å	13.876(3)	13.583(5)	13.8998(17)
α / deg	105.43(2)	107.691(10)	105.625(7)
β / deg	114.02(3)	110.472(10)	113.161(7)
γ / deg	100.40(2)	98.339(10)	100.582(8)
V/ Å ³	1851.5(11)	1785.2(11)	1888.9(4)
Z	1	1	1
limiting indices	-15 ≤ h ≤ 15 -15 ≤ k ≤ 15 -17 ≤ l ≤ 17	-14 ≤ h ≤ 14 -15 ≤ k ≤ 15 -15 ≤ l ≤ 16	-14 ≤ h ≤ 15 -15 ≤ k ≤ 15 -16 ≤ l ≤ 16
D _c /g cm ⁻³	1.757	1.756	1.727
μ (mm ⁻¹)	3.071	3.070	3.127
F(000)	986	944	988
T/K	150	296	299
Total reflections	27488	15733	18061
R(int)	0.0450	0.0747	0.0804
Unique reflections	7581	6838	6678
Observed reflections	6788	4280	4699
Parameters	486	464	486
R _i ; wR ₂ (I > 2 σ (I))	0.0266, 0.0669	0.0590, 0.1904	0.0714, 0.1966
GOF (F ²)	1.033	1.035	1.053
Largest diff peak and hole (e Å ⁻³)	1.068, -0.632	1.676, -1.503	4.371, -1.427
CCDC No.	2005017	2005018	2005019

parameters	4	5	6
Formula	C ₆₈ H ₇₈ Dy ₂ Mn ₂ N ₆ Ni ₂ O ₃₀	C ₆₈ H ₇₈ Tb ₂ Mn ₂ N ₆ Ni ₂ O ₃₀	C ₆₈ H ₇₈ Ho ₂ Mn ₂ N ₆ Ni ₂ O ₃₀
F.W. (g mol ⁻¹)	2011.66	2004.48	2016.49
crystal system	monoclinic	monoclinic	monoclinic
space group	P 2 ₁ /n	P 2 ₁ /n	P 2 ₁ /n
Crystal color	Greenish brown	Greenish brown	Greenish brown
Crystal size/mm ³	0.18×0.14×0.10	0.21×0.12×0.08	0.20×0.16×0.13
a/ Å	11.938(2)	11.954(5)	11.9904(8)
b/ Å	24.563(5)	24.543(7)	24.7140(16)
c/ Å	13.784(3)	13.797(4)	13.8321(9)
α/ deg	90.00(3)	90.00(2)	90.00
β/ deg	111.96(3)	112.06(2)	112.164(2)
γ/ deg	90.00(3)	90.00(2)	90.00
V/ Å ³	3748.6(15)	3734.2(15)	3796.0(4)
Z	2		2
limiting indices	-14 ≤ h ≤ 15 -31 ≤ k ≤ 30 -17 ≤ l ≤ 17		-14 ≤ h ≤ 14 -29 ≤ k ≤ 29 -16 ≤ l ≤ 16
D _c /g cm ⁻³	1.782		1.764
μ (mm ⁻¹)	2.876		2.956
F(000)	2012		2016
T/K	150(2)		150(2)
Total reflections	47899		26196
R(int)	0.0601		0.0766
Unique reflections	7874		6669
Observed reflections	6480		5600
Parameters	502		502
R _i ; wR ₂ (I > 2σ(I))	0.0380, 0.0968		0.0495, 0.1523
GOF (F ²)	1.046		1.114
Largest diff peak and hole (e Å ⁻³)	1.730, -0.706		1.686, -0.973
CCDC No.	2005020	-	2005021

Chart 1 Binding Sites and Coordination modes of L²⁻, AcO⁻ and HO⁻

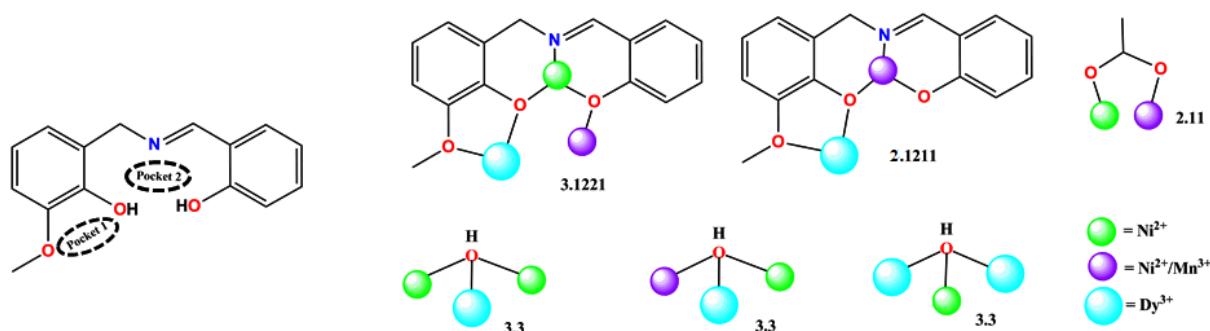


Table S2 Results of continuous shape measures calculations^{S1-S3} using program SHAPE 2.1 for Ni^{II} atoms of **1-3**.^a

	JPPY-6	TPR-6	OC-6	PPY-6	HP-6
Ni1 of 1	28.684	13.230	0.873	25.789	31.921
Ni2 of 1	27.122	12.424	0.819	23.247	29.217
Ni1 of 2	29.479	13.749	0.658	26.505	31.877
Ni2 of 2	26.834	12.496	0.870	22.917	29.387
Ni1 of 3	29.058	13.501	0.866	26.248	31.516
Ni2 of 3	27.158	12.319	0.845	23.238	29.389

Table S3 Results of continuous shape measures calculations^{S1-S3} using program SHAPE 2.1 for Ni^{II} and Mn^{III} atoms of **4-6**.^a

	JPPY-6	TPR-6	OC-6	PPY-6	HP-6
Ni1 of 4	26.744	11.902	0.996	22.692	29.349
Mn1 of 4	29.645	13.759	1.139	26.671	32.582
Ni1 of 6	26.704	11.827	0.992	22.708	29.248
Mn1 of 6	29.542	13.609	1.159	26.629	32.593

^aJPPY-6 = Johnson pentagonal pyramid J2, TPR-6 = Trigonal prism, OC-6 = Octahedron, PPY-6 = Pentagonal pyramid, HP-6 = Hexagon

Table S4 Results of continuous shape measures calculations^{S1-S3} using program SHAPE 2.1 for Ln^{III} atoms of **1-6**.^a

[ML8]	OP-8	HPY-8	HBPY-8	CU-8	SAPR-8	TDD-8	JGBF-8	JETBPY-8	JBTPR-8	BTPR-8	JSD-8	TT-8
Dy1 of 1	31.899	21.592	13.644	7.459	2.334	1.280	14.827	26.624	2.922	2.669	3.432	7.803
Tb1 of 2	32.209	21.430	13.565	7.582	2.594	1.373	14.570	26.725	2.923	2.691	3.458	7.854

Ho1 of 3	32.079	21.601	13.660	7.431	2.394	1.212	14.561	26.760	2.888	2.688	3.251	7.709
Dy1 of 4	32.122	20.485	13.216	8.054	2.024	1.339	14.284	26.899	2.965	2.920	3.466	8.397
Ho1 of 6	32.093	20.598	13.250	8.019	2.017	1.292	14.271	26.937	2.898	2.938	3.400	8.356

^aOP-8 = Octagon, HPY-8 = Heptagonal pyramid, HBPY-8 = Hexagonal bipyramid, CU-8 = Cube, SAPR-8 = square antiprism, TDD-8 = Triangular dodecahedron, JGBF-8 = Johnson gyrobifastigium J26, JETBPY-8 = Johnson elongated triangular bipyramid J14, JBTPR-8 = Biaugmented trigonal prism J50, BTPR-8 = Biaugmented trigonal prism, JSD-8 = Snub diphenoid J84, TT-8 = Triakis tetrahedron

Table S5 BVS calculation for the Mn metal ion of complex **4** and **6**

Complex	Mn ^{II}	Mn ^{III}	Mn ^{IV}
Mn1 of 4	3.235	2.994	3.087
Mn1 of 6	3.237	2.995	3.086

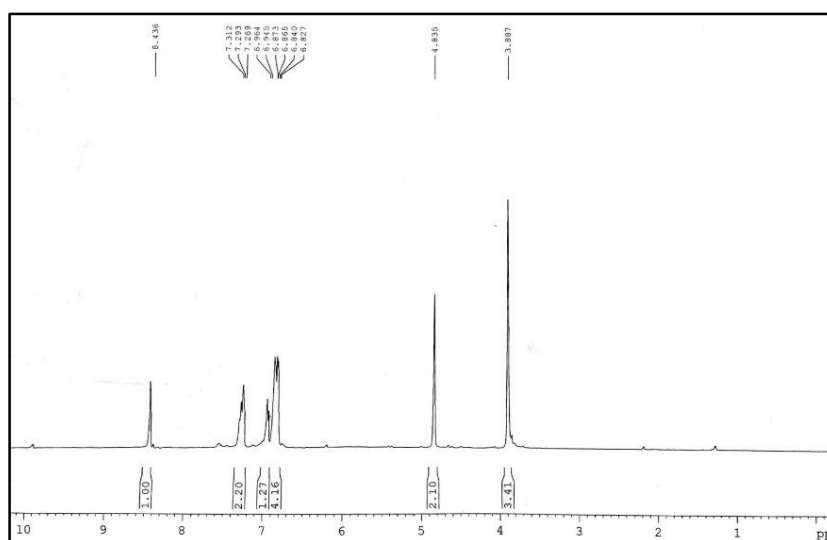


Figure S1. ¹H NMR spectrum of H₂L

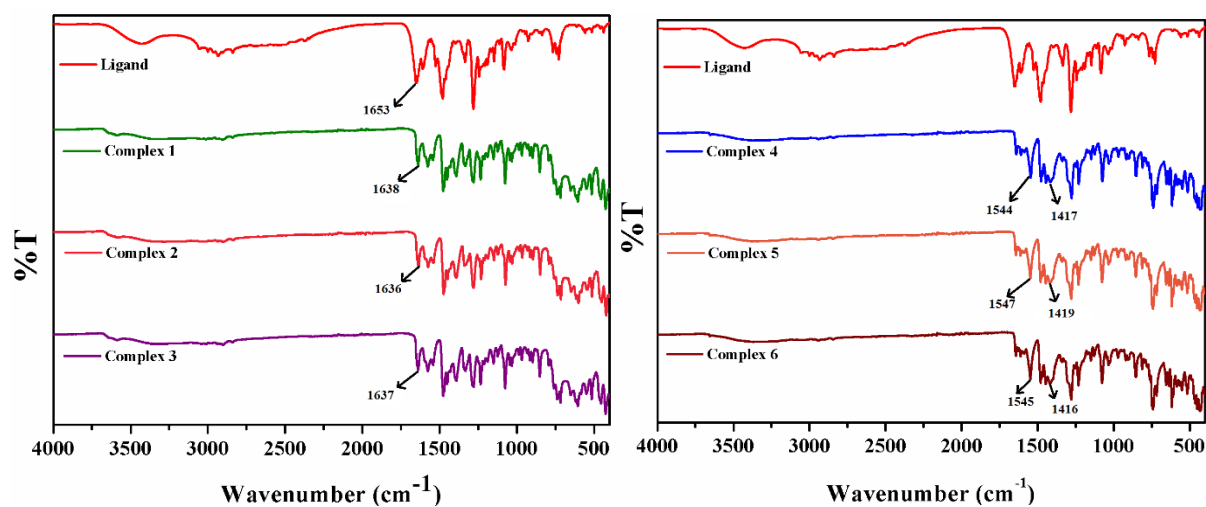


Figure S2. *Left:* FTIR spectra of H₂L, Complex **1**, **2** and **3**; *Right:* FTIR spectra of H₂L, Complex **4**, **5** and **6**

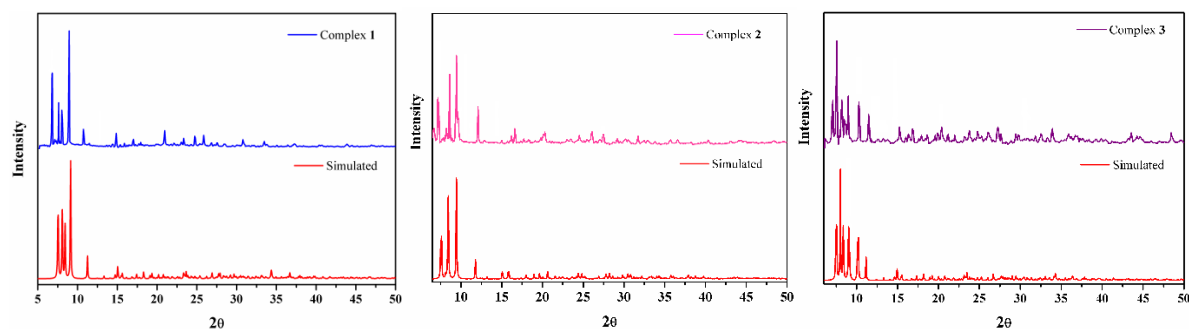


Figure S3. PXRD patterns of Complexes 1–3

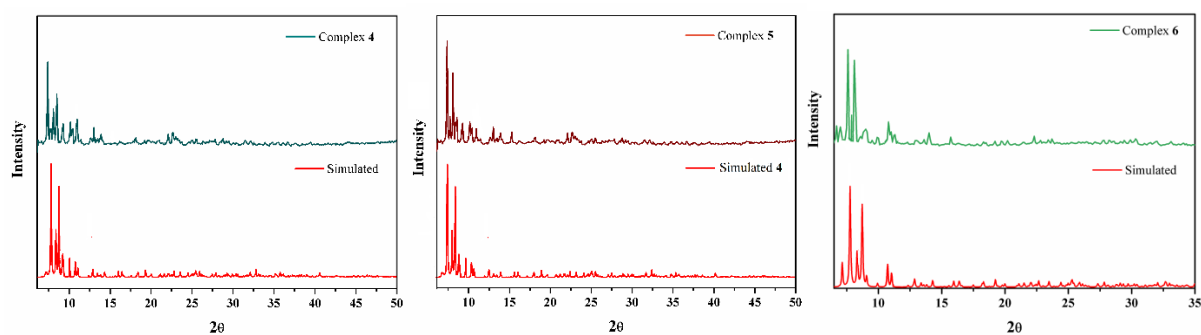


Figure S4. PXRD patterns of Complexes 4–6

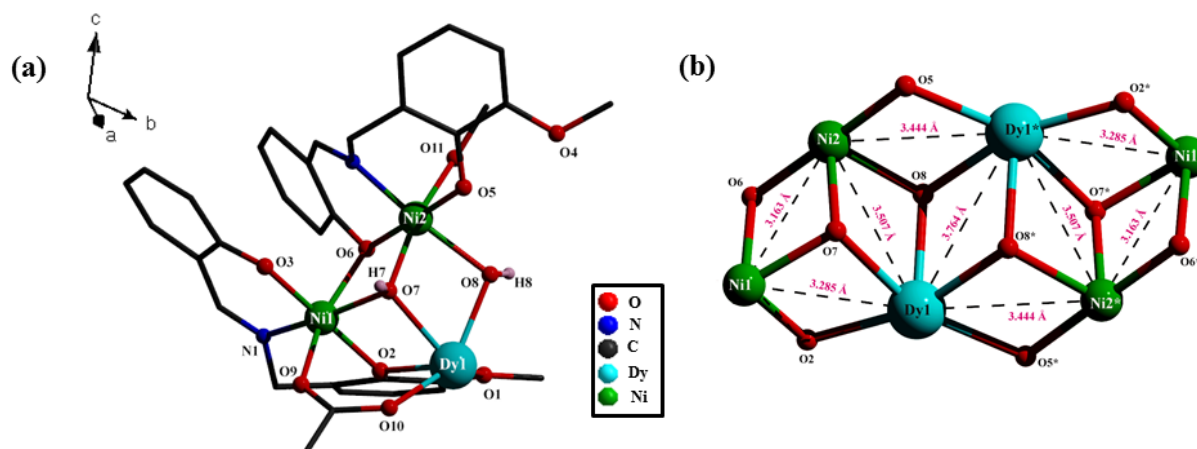


Figure S5. (a) Asymmetric unit of complex 1 with partial atom numbering scheme. (b) Core structure of complex 1 showing intra-metal atom separations with atom numbering scheme.

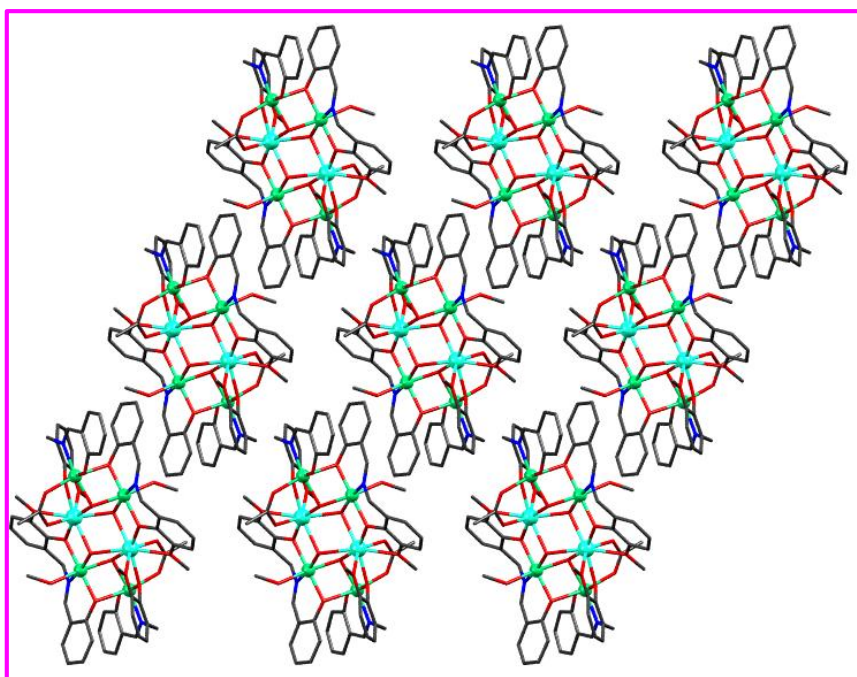


Figure S6. Crystal packing of **1** along crystallographic b axis

Table S6 Selected bond distances of **1**

Atom 1	Atom 2	Distance [Å]	Atom 1	Atom 2	Distance [Å]
Dy1	O2	2.239(3)	Ni1	O2	2.018(2)
Dy1	O5*	2.294(2)	Ni1	O7	2.045(2)
Dy1	O10	2.316(2)	Ni1	O9	2.104(2)
Dy1	O7	2.343(2)	Ni1	O6	2.307(2)
Dy1	O8*	2.357(2)	Ni2	N2	2.015(3)
Dy1	O8	2.359(2)	Ni2	O5	2.022(2)
Dy1	O4*	2.571(2)	Ni2	O6	2.025(2)
Dy1	O1	2.595(2)	Ni2	O7	2.027(2)
Ni1	O3	1.983(2)	Ni2	O11	2.148(2)
Ni1	N1	1.997(3)	Ni2	O8	2.155(2)

Table S7 Selected bond angles of **1**

Atom 1	Atom 2	Atom 3	Bond Angles(°)	Atom 1	Atom 2	Atom 3	Bond Angles(°)
O2	Dy1	O5*	127.21(8)	O2	Ni1	O7	85.80(9)

O2	Dy1	O10	84.25(9)		O3	Ni1	O9	88.45(10)
O5*	Dy1	O10	107.36(8)		N1	Ni1	O9	98.89(10)
O2	Dy1	O7	74.25(8)		O2	Ni1	O9	88.88(9)
O5*	Dy1	O7	158.25(7)		O7	Ni1	O9	91.14(9)
O10	Dy1	O7	75.52(8)		O3	Ni1	O6	99.75(9)
O2	Dy1	O8*	160.27(8)		N1	Ni1	O6	92.61(10)
O5*	Dy1	O8*	72.52(8)		O2	Ni1	O6	82.56(9)
O10	Dy1	O8*	90.08(8)		O7	Ni1	O6	77.03(9)
O7	Dy1	O8*	86.04(8)		O9	Ni1	O6	165.82(8)
O2	Dy1	O8	99.12(8)		N2	Ni2	O5	90.57(10)
O5*	Dy1	O8	100.42(8)		N2	Ni2	O6	89.23(10)
O10	Dy1	O8	142.13(8)		O5	Ni2	O6	179.61(10)
O7	Dy1	O8	69.36(8)		N2	Ni2	O7	102.29(10)
O8	Dy1	O8*	74.10(9)		O5	Ni2	O7	95.48(9)
O2	Dy1	O4*	72.37(8)		O6	Ni2	O7	84.23(9)
O5*	Dy1	O4*	63.55(8)		N2	Ni2	O11	90.05(10)
O10	Dy1	O4*	72.45(8)		O5	Ni2	O11	91.59(10)
O7	Dy1	O4*	135.36(8)		O6	Ni2	O11	88.75(9)
O8*	Dy1	O4*	123.78(8)		O7	Ni2	O11	165.68(9)
O8	Dy1	O4*	144.66(7)		N2	Ni2	O8	172.83(10)
O2	Dy1	O1	64.43(8)		O5	Ni2	O8	82.32(9)
O5*	Dy1	O1	74.47(8)		O6	Ni2	O8	97.88(9)
O10	Dy1	O1	137.26(8)		O7	Ni2	O8	79.47(9)
O7	Dy1	O1	118.64(8)		O11	Ni2	O8	89.19(9)
O8*	Dy1	O1	128.71(8)		Ni2	O7	Ni1	101.92(10)
O8	Dy1	O1	74.61(8)		Ni2	O7	Dy1	106.54(9)
O4*	Dy1	O1	70.81(8)		Ni1	O7	Dy1	96.71(9)
O3	Ni1	N1	90.62(11)		Ni2	O6	Ni1	93.59(9)
O3	Ni1	O2	176.93(9)		Ni1	O2	Dy1	100.89(9)

N1	Ni1	O2	91.28(11)		Ni2	O8	Dy1*	99.43(9)
O3	Ni1	O7	92.74(9)		Ni2	O8	Dy1	101.88(9)
N1	Ni1	O7	169.51(10)		Dy1	O8	Dy1*	105.90(9)

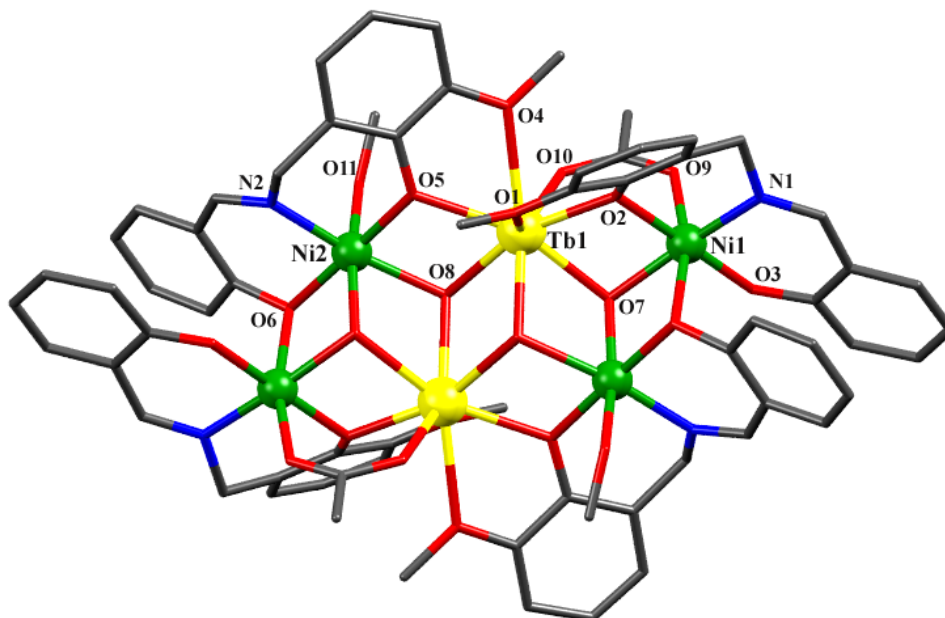


Figure S7. Molecular structure of Complex **2** with partial atomic numbering scheme. Solvent molecules are omitted for clarity.

Table S8 Selected bond distances of **2**

Atom 1	Atom 2	Distance [Å]	Atom 1	Atom 2	Distance [Å]
Tb1	O4	2.544(6)	Ni1	O3	1.975(7)
Tb1	O8*	2.338(6)	Ni1	O2	2.006(6)
Tb1	O8	2.386(6)	Ni1	O9	2.079(6)
Tb1	O7	2.360(6)	Ni1	N1	2.001(8)
Tb1	O1	2.619(7)	Ni2	O8	2.151(6)
Tb1	O2	2.243(6)	Ni2	O6	2.012(6)
Tb1	O5	2.314(6)	Ni2	O7	2.009(6)
Tb1	O10	2.303(6)	Ni2	N2	2.016(8)
Ni1	O6	2.236(6)	Ni2	O5	2.014(6)
Ni1	O7	2.033(5)	Ni2	O11	2.148(7)

Table S9 Selected bond angles of **2**

Atom 1	Atom 2	Atom 3	Bond Angles(°)	Atom 1	Atom 2	Atom 3	Bond Angles(°)
O4	Tb1	O1	70.1(2)	O7	Ni1	O6	78.0(2)
O10	Tb1	O4	73.4(2)	O3	Ni1	N1	91.3(3)
O10	Tb1	O8	92.8(2)	O3	Ni1	O9	88.3(3)
O10	Tb1	O8*	142.9(2)	O3	Ni1	O6	98.9(3)
O10	Tb1	O7	75.6(2)	O3	Ni1	O7	91.9(2)
O10	Tb1	O1	137.1(2)	O3	Ni1	O2	176.2(3)
O8*	Tb1	O4	142.3(2)	O2	Ni1	N1	91.4(3)
O8	Tb1	O4	124.8(2)	O2	Ni1	O9	88.7(3)
O8	Tb1	O8*	74.3(2)	O2	Ni1	O6	83.7(2)
O8*	Tb1	O1	72.8(2)	O2	Ni1	O7	85.8(2)
O8	Tb1	O1	126.57(19)	O6	Ni2	O11	88.7(3)
O7	Tb1	O4	135.54(19)	O6	Ni2	O8	98.8(2)
O7	Tb1	O8*	69.3(2)	O6	Ni2	O7	84.1(2)
O7	Tb1	O8	87.60(19)	O6	Ni2	O5	178.9(3)
O7	Tb1	O1	117.4(2)	O7	Ni2	O11	165.1(3)
O2	Tb1	O4	72.7(2)	O7	Ni2	O8	79.8(2)
O2	Tb1	O10	84.6(2)	O7	Ni2	O5	96.3(2)
O2	Tb1	O8*	96.5(2)	N2	Ni2	O11	91.6(3)
O2	Tb1	O8	160.8(2)	N2	Ni2	O8	171.9(3)
O2	Tb1	O7	73.3(2)	N2	Ni2	O6	89.3(3)
O2	Tb1	O1	63.7(2)	N2	Ni2	O7	101.3(3)
O2	Tb1	O5	127.5(2)	N2	Ni2	O5	89.6(3)
O5	Tb1	O4	63.7(2)	O5	Ni2	O11	91.1(3)
O5	Tb1	O10	108.3(2)	O5	Ni2	O8	82.3(2)
O5	Tb1	O8*	100.3(2)	Tb1	O8	Tb1*	105.7(2)
O5	Tb1	O8	71.4(2)	Ni2	O8	Tb1*	102.4(2)
O5	Tb1	O7	158.7(2)	Ni2	O8	Tb1	99.8(2)
O5	Tb1	O1	74.6(2)	Ni2	O6	Ni1	94.4(3)

N1	Ni1	O9	97.5(3)		Ni2*	O7	Tb1	106.2(2)
N1	Ni1	O6	93.3(3)		Ni2	O7	Ni1*	101.1(3)
N1	Ni1	O7	171.1(3)		Ni1	O7	Tb1	96.9(2)
O9	Ni1	O6	166.9(2)		Ni1	O2	Tb1	101.5(3)
O7	Ni1	O9	90.9(2)		Ni2	O5	Tb1	106.5(3)

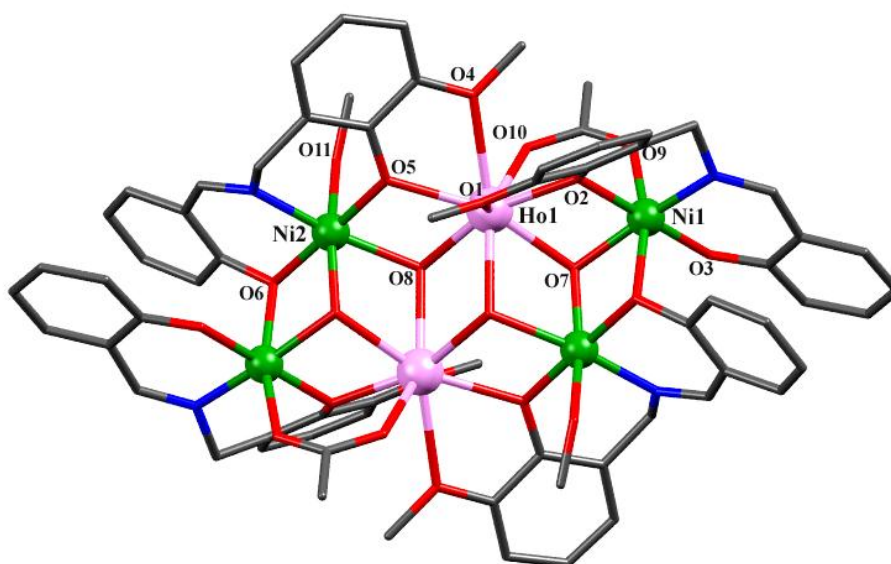


Figure S8. Molecular structure of Complex **3** with partial atomic numbering scheme. Solvent molecules are omitted for clarity.

Table S10 Selected bond distances of **3**

Atom 1	Atom 2	Distance [Å]	Atom 1	Atom 2	Distance [Å]
Ho1	O4	2.574(7)	Ni1	O3	1.982(8)
Ho1	O8*	2.329(8)	Ni1	O2	2.016(7)
Ho1	O8	2.362(7)	Ni1	O9	2.093(8)
Ho1	O7	2.342(7)	Ni1	N1	2.003(9)
Ho1	O1	2.602(8)	Ni2	O8	2.162(7)
Ho1	O2	2.247(7)	Ni2	O6	2.015(7)
Ho1	O5	2.287(7)	Ni2	O7	2.036(8)
Ho1	O10	2.287(8)	Ni2	N2	2.026(9)
Ni1	O6	2.336(9)	Ni2	O5	2.036(7)
Ni1	O7	2.056(7)	Ni2	O11	2.151(10)

Table S11 Selected bond angles of **3**

Atom 1	Atom 2	Atom 3	Bond Angles(°)	Atom 1	Atom 2	Atom 3	Bond Angles(°)
O4	Ho1	O1	71.0(3)	O7	Ni1	O6	77.1(3)
O10	Ho1	O4	72.6(3)	O3	Ni1	N1	91.3(4)
O10	Ho1	O8	89.7(3)	O3	Ni1	O9	89.0(4)
O10	Ho1	O8*	142.2(3)	O3	Ni1	O6	99.6(3)
O10	Ho1	O7	75.4(3)	O3	Ni1	O7	92.4(3)
O10	Ho1	O1	137.9(3)	O3	Ni1	O2	177.7(3)
O8*	Ho1	O4	144.5(3)	O2	Ni1	N1	90.8(4)
O8	Ho1	O4	124.3(3)	O2	Ni1	O9	89.7(3)
O8	Ho1	O8*	73.6(3)	O2	Ni1	O6	81.3(3)
O8*	Ho1	O1	74.3(3)	O2	Ni1	O7	85.7(3)
O8	Ho1	O1	128.6(3)	O6	Ni2	O11	88.4(4)
O7	Ho1	O4	135.1(2)	O6	Ni2	O8	98.6(3)
O7	Ho1	O8*	69.8(2)	O6	Ni2	O7	85.3(3)
O7	Ho1	O8	85.6(2)	O6	Ni2	O5	179.5(3)
O7	Ho1	O1	118.6(3)	O7	Ni2	O11	165.4(3)
O2	Ho1	O4	72.7(3)	O7	Ni2	O8	79.0(3)
O2	Ho1	O10	85.5(3)	O7	Ni2	O5	94.5(3)
O2	Ho1	O8*	98.5(3)	N2	Ni2	O11	91.0(4)
O2	Ho1	O8	159.9(2)	N2	Ni2	O8	172.3(3)
O2	Ho1	O7	74.2(2)	N2	Ni2	O6	89.0(3)
O2	Ho1	O1	63.9(3)	N2	Ni2	O7	102.1(4)
O2	Ho1	O5	127.6(2)	N2	Ni2	O5	90.6(3)
O5	Ho1	O4	63.7(2)	O5	Ni2	O11	91.8(3)
O5	Ho1	O10	106.7(3)	O5	Ni2	O8	81.8(3)
O5	Ho1	O8*	100.3(3)	Ho1	O8	Ho1*	106.4(3)
O5	Ho1	O8	72.5(2)	Ni2	O8	Ho1*	102.2(3)
O5	Ho1	O7	158.0(2)	Ni2	O8	Ho1	99.6(3)
O5	Ho1	O1	75.1(3)	Ni2	O6	Ni1	93.2(3)

N1	Ni1	O9	98.2(4)		Ni2*	O7	Ho1	105.8(3)
N1	Ni1	O6	93.0(4)		Ni2	O7	Ni1*	101.4(3)
N1	Ni1	O7	169.8(4)		Ni1	O7	Ho1	96.5(3)
O9	Ni1	O6	165.8(3)		Ni1	O2	Ho1	100.8(3)
O7	Ni1	O9	91.3(3)		Ni2	O5	Ho1	106.1(3)

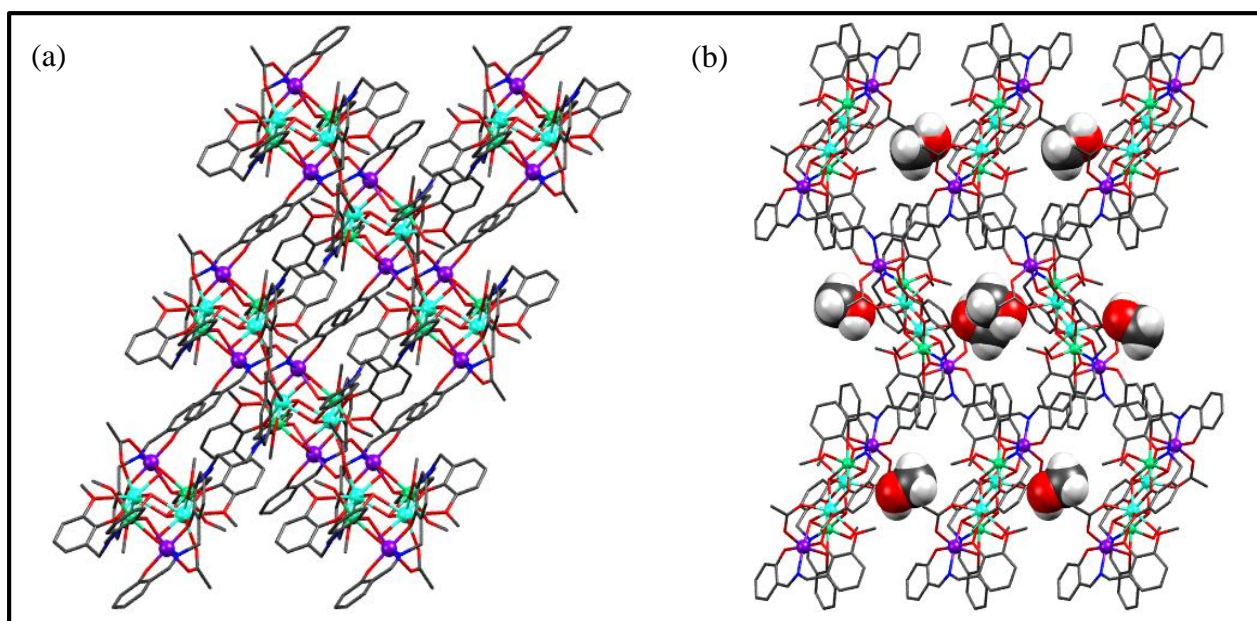


Figure S9. (a) Crystal packing of **4** along crystallographic b axis. (b) Zigzag crystal packing of **4** along crystallographic c axis with solvent methanol in the void position.

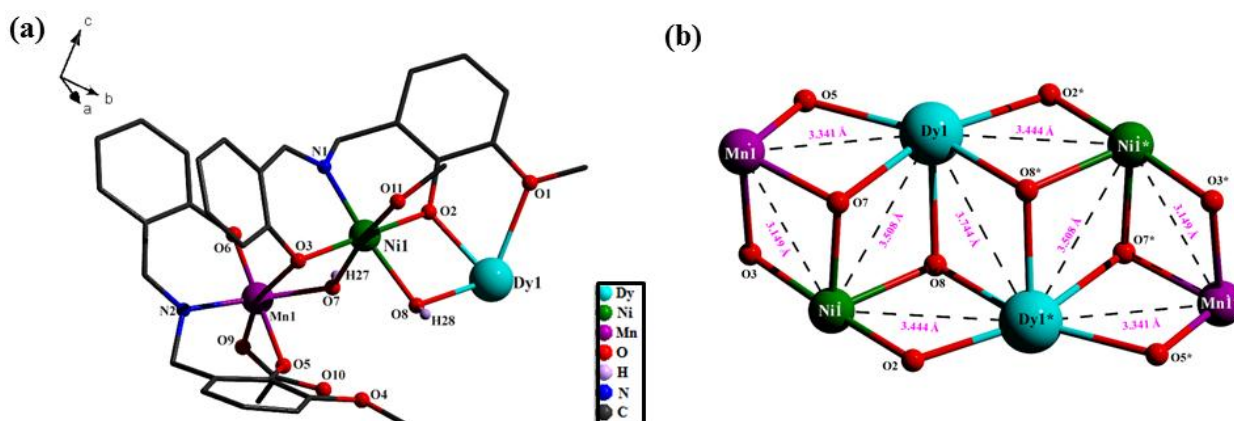


Figure S10. (a) Asymmetric unit of complex **4** with partial atom numbering scheme (b) Core structure of complex **1** with intra-metallic bond distances with atom numbering scheme

Table S12 Selected bond distances of **4**

Atom 1	Atom 2	Distance [Å]		Atom 1	Atom 2	Distance [Å]
Dy1	O2	2.259(3)		Ni1	O2	2.031(3)
Dy1	O10	2.279(3)		Ni1	O7	2.074(3)
Dy1	O5	2.318(3)		Ni1	O11	2.119(3)
Dy1	O8*	2.321(3)		Ni1	O8	2.150(3)
Dy1	O8	2.342(3)		Mn1	O6	1.861(3)
Dy1	O7	2.383(3)		Mn1	O5	1.932(3)
Dy1	O4	2.528(3)		Mn1	O7	1.957(3)
Dy1	O1	2.565(3)		Mn1	N2	2.009(4)
Ni1	O3	2.006(3)		Mn1	O9	2.189(3)
Ni1	N1	2.014(4)		Mn1	O3	2.252(3)

Table S13 Selected bond angles of **4**

Atom 1	Atom 2	Atom 3	Bond Angles(°)		Atom 1	Atom 2	Atom 3	Bond Angles(°)
O2	Dy1	O10*	105.07(12)		O3	Ni1	O11	90.93(12)
O2	Dy1	O5*	132.18(11)		N1	Ni1	O11	93.27(14)
O10	Dy1*	O5	81.39(11)		O2	Ni1	O11	94.08(12)
O2	Dy1	O8*	100.46(11)		O7	Ni1	O11	164.84(12)
O10	Dy1*	O8	142.13(12)		O3	Ni1	O8	99.79(12)
O5	Dy1*	O8	101.56(10)		N1	Ni1	O8	171.29(13)
O2	Dy1	O8	72.34(11)		O2	Ni1	O8	80.99(12)
O10*	Dy1	O8	88.38(11)		O7	Ni1	O8	79.80(12)
O5*	Dy1	O8	155.15(11)		O11	Ni1	O8	89.11(12)
O8	Dy1	O8*	73.20(11)		O6	Mn1	O5	177.29(13)
O2	Dy1	O7*	158.82(10)		O6	Mn1	O7	92.17(13)
O10	Dy1*	O7	75.91(11)		O5	Mn1	O7	86.45(13)
O5	Dy1*	O7	68.99(10)		O6	Mn1	N2	90.77(15)
O8	Dy1*	O7	70.34(10)		O5	Mn1	N2	90.79(14)
O8	Dy1	O7*	86.61(10)		O7	Mn1	N2	174.74(1)

O2	Dy1	O4*	80.11(10)		O6	Mn1	O9	92.50(14)
O10	Dy1*	O4	136.18(11)		O5	Mn1	O9	85.12(13)
O5	Dy1*	O4	65.46(10)		O7	Mn1	O9	88.02(12)
O8	Dy1*	O4	75.28(10)		N2	Mn1	O9	96.20(14)
O8	Dy1	O4*	132.91(10)		O6	Mn1	O3	98.50(13)
O7	Dy1*	O4	114.27(10)		O5	Mn1	O3	83.49(12)
O1	Dy1	O2	64.13(10)		O7	Mn1	O3	77.63(11)
O1	Dy1	O10*	73.62(12)		N2	Mn1	O3	97.63(13)
O1	Dy1	O5*	73.15(10)		O9	Mn1	O3	162.17(11)
O1	Dy1	O8*	143.78(11)		Ni1	O2	Dy1	106.65(13)
O1	Dy1	O8	125.48(10)		Ni1	O3	Mn1	95.20(12)
O1	Dy1	O7*	134.10(10)		Mn1	O5	Dy1*	103.25(13)
O1	Dy1	O4*	69.97(11)		Mn1	O7	Ni1	102.72(13)
O3	Ni1	N1	88.55(14)		Mn1	O7	Dy1*	100.20(12)
O3	Ni1	O2	174.95(12)		Ni1	O7	Dy1	103.58(12)
N1	Ni1	O2	90.47(14)		Ni1	O8	Dy1*	103.31(12)
O3	Ni1	O7	80.91(12)		Ni1	O8	Dy1	100.02(12)
N1	Ni1	O7	99.23(14)		Dy1	O8	Dy1*	106.80(11)
O2	Ni1	O7	94.36(12)					

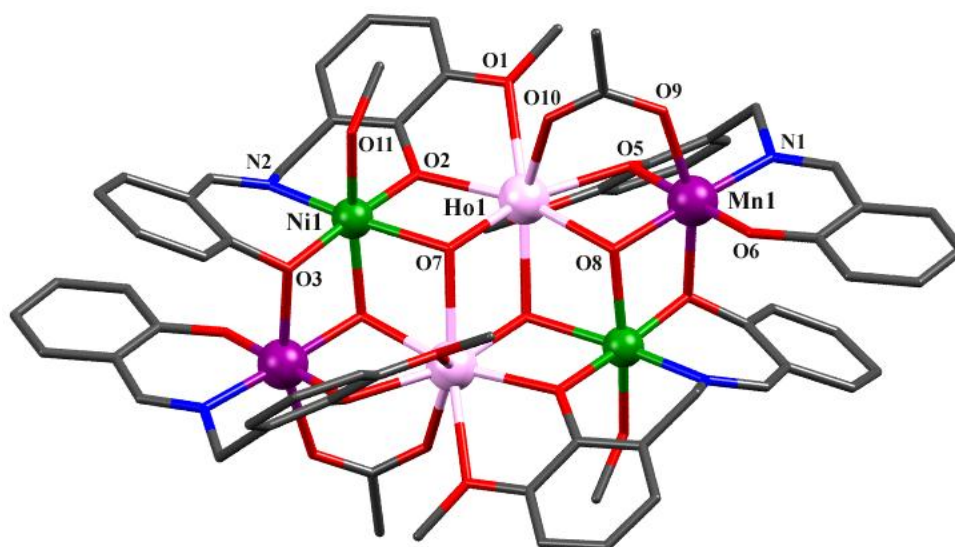


Figure S11. Molecular structure of Complex **6** with partial atomic numbering scheme. Solvent molecules and counter anions are omitted for clarity.

Table S14 Selected bond distances of **6**

Atom 1	Atom 2	Distance [Å]		Atom 1	Atom 2	Distance [Å]
Ho1	O2	2.251(4)		Ni1	O2	2.040(4)
Ho1	O10	2.271(5)		Ni1	O8	2.076(4)
Ho1	O5	2.315(4)		Ni1	O11	2.116(5)
Ho1	O8	2.390(4)		Ni1	O7	2.158(4)
Ho1	O7	2.328(4)		Mn1	O6	1.859(5)
Ho1	O7*	2.323(4)		Mn1	O5	1.930(5)
Ho1	O4	2.523(5)		Mn1	O8	1.960(4)
Ho1	O1	2.569(5)		Mn1	N1	2.006(5)
Ni1	O3	2.020(4)		Mn1	O9	2.191(5)
Ni1	N2	2.023(6)		Mn1	O3	2.260(4)

Table S15 Selected bond angles of **6**

Atom 1	Atom 2	Atom 3	Bond Angles(°)		Atom 1	Atom 2	Atom 3	Bond Angles(°)
O2	Ho1	O10	104.66(17)		O3	Ni1	O11	90.88(18)
O2	Ho1	O5	132.02(15)		N2	Ni1	O11	92.8(2)
O10	Ho1	O5	81.63(17)		O2	Ni1	O11	94.25(18)
O2	Ho1	O7	100.49(15)		O8*	Ni1	O11	165.11(18)
O10	Ho1	O7*	142.27(18)		O3	Ni1	O7	100.06(17)
O5	Ho1	O7	101.75(15)		N2	Ni1	O7	171.2(2)
O2	Ho1	O7	72.73(15)		O2	Ni1	O7	80.56(16)
O10	Ho1	O7	88.00(17)		O8*	Ni1	O7	79.98(16)
O5	Ho1	O7	154.89(16)		O11	Ni1	O7	89.22(17)
O7	Ho1	O7*	73.10(16)		O6	Mn1	O5	177.4(2)
O2	Ho1	O8	158.92(15)		O6	Mn1	O8	92.04(19)
O10	Ho1	O8	76.03(16)		O5	Mn1	O8	86.57(18)
O5	Ho1	O8	69.06(15)		O6	Mn1	N1	90.7(2)
O7*	Ho1	O8	70.53(15)		O5	Mn1	N1	90.9(2)
O7	Ho1	O8	86.30(14)		O8	Mn1	N1	174.5(2)

O2	Ho1	O4	80.14(16)		O6	Mn1	O9	92.7(2)
O10	Ho1	O4	136.19(17)		O5	Mn1	O9	85.09(19)
O5	Ho1	O4	65.38(15)		O8	Mn1	O9	88.16(18)
O7*	Ho1	O4	75.41(15)		N1	Mn1	O9	96.5(2)
O7	Ho1	O4	133.25(15)		O6	Mn1	O3*	98.93(19)
O8	Ho1	O4	114.37(15)		O5	Mn1	O3*	82.94(17)
O2	Ho1	O1	64.36(15)		O8	Mn1	O3*	77.86(16)
O10	Ho1	O1	73.22(18)		N1	Mn1	O3*	97.0(2)
O5	Ho1	O1	72.81(15)		O9	Mn1	O3*	162.07(17)
O7*	Ho1	O1	144.07(17)		Ni1	O2	Ho1	106.56(18)
O7	Ho1	O1	125.81(16)		Mn1	O5	Ho1	103.35(18)
O8	Ho1	O1	133.63(15)		Ni1	O3	Mn1*	94.83(17)
O4	Ho1	O1	70.08(17)		Mn1	O8	Ni1*	102.81(19)
O3	Ni1	N2	88.4(2)		Mn1	O8	Ho1	99.82(17)
O3	Ni1	O2	174.85(18)		Ni1*	O8	Ho1	103.30(17)
N2	Ni1	O2	90.8(2)		Ni1	O7	Ho1*	102.98(18)
O3	Ni1	O8*	81.05(17)		Ni1	O7	Ho1	100.16(18)
N2	Ni1	O8*	99.38(19)		Ho1	O7	Ho1*	106.90(16)
O2	Ni1	O8*	94.06(17)					

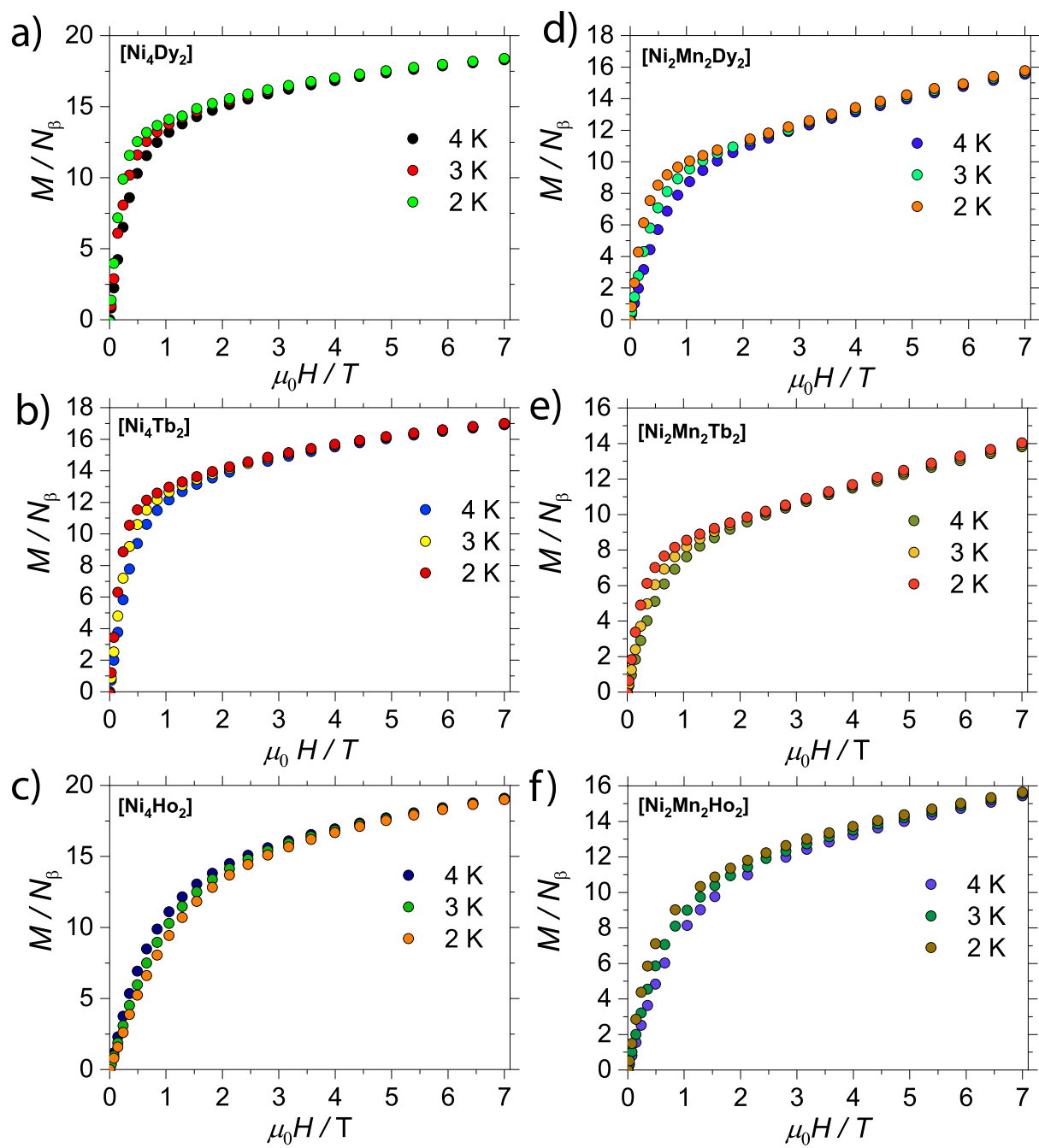


Figure S12. Magnetisation vs Field data for all complexes in the temperature range of 2 to 4 K and a field range of 0 to 7 T.

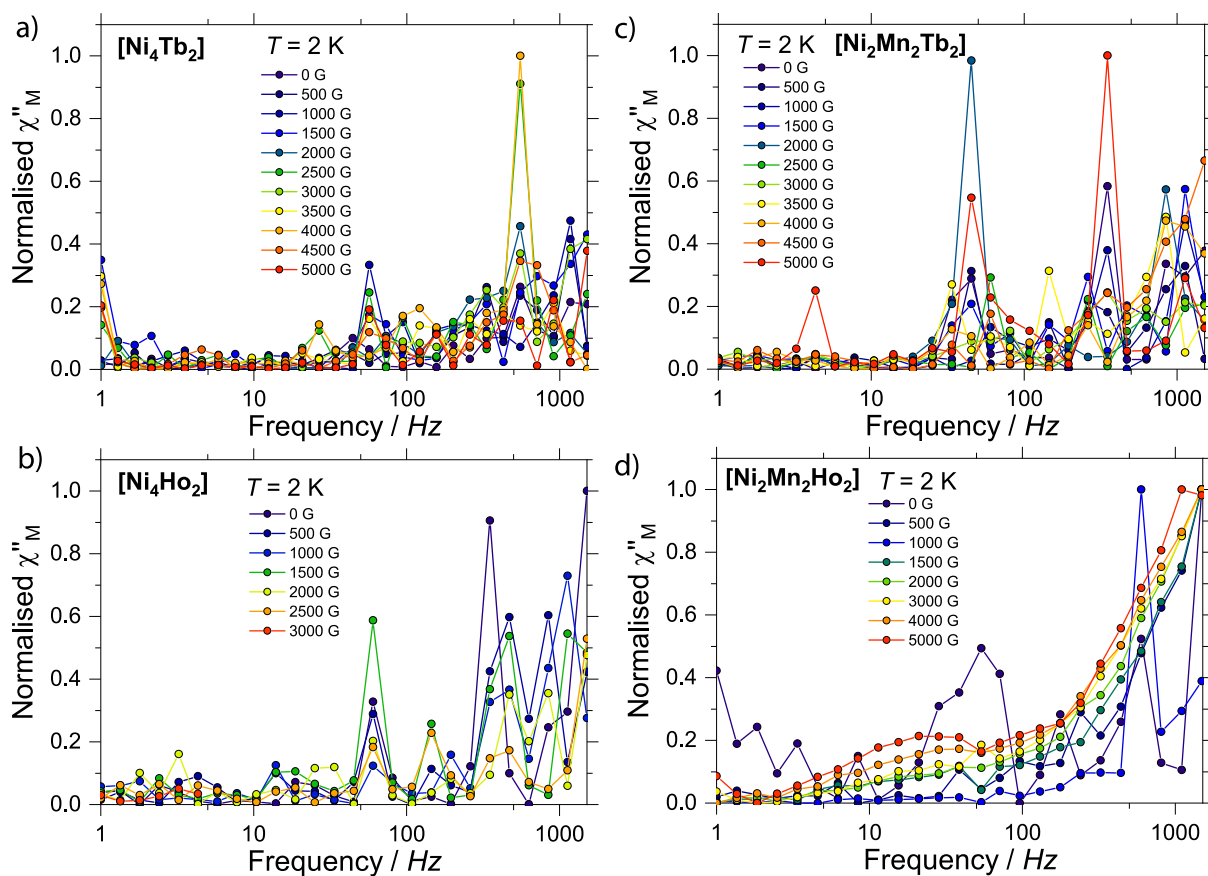


Figure S13. Field and frequency dependent AC susceptibility study for complexes **2**, **3**, **5** and **6**. As shown in the AC data, none of the complexes show a maxima in the χ_M'' in the frequency and field range of study.

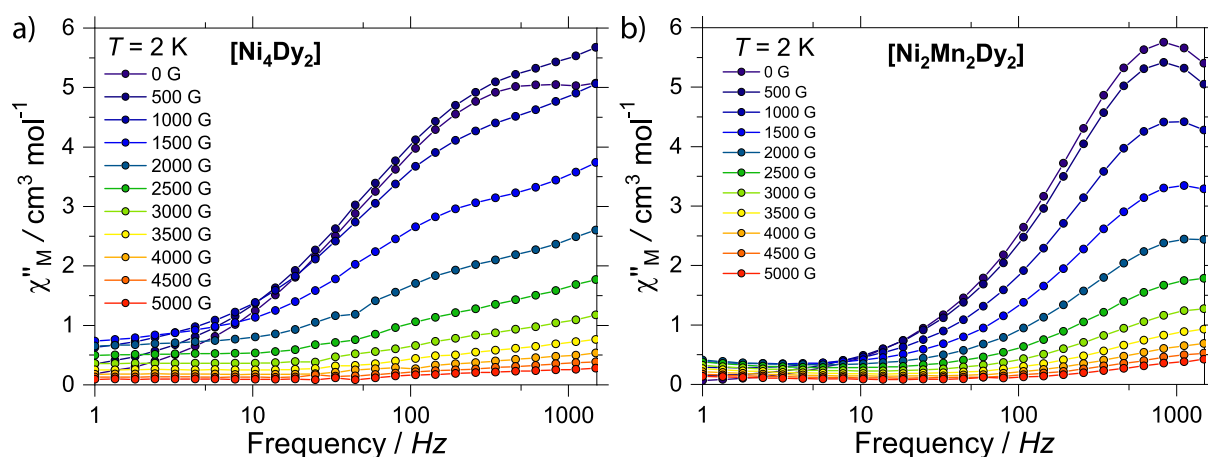


Figure S14. Field dependent out-of-phase magnetic susceptibility study at 2 K conducted on a) Complex **1** and b) Complex **4**. As shown in the data, application of a DC does not decrease relaxation.

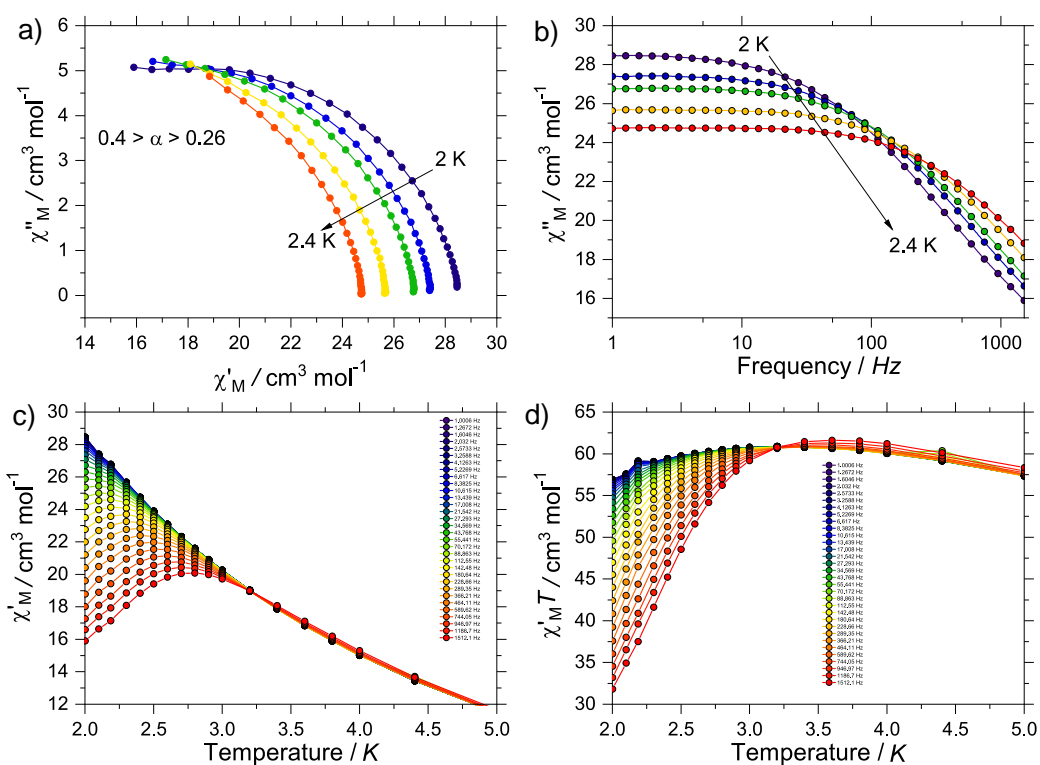


Figure S15. a) Cole-Cole plots for complex **1**; b) Experimental $\chi_M''(\nu)$ with $H_{DC} = 0$ for complex **1**; c) and d) are the experimental $\chi_M'(T)$ and $\chi_M'T(T)$ data for the **Ni₄Dy₂** complex.

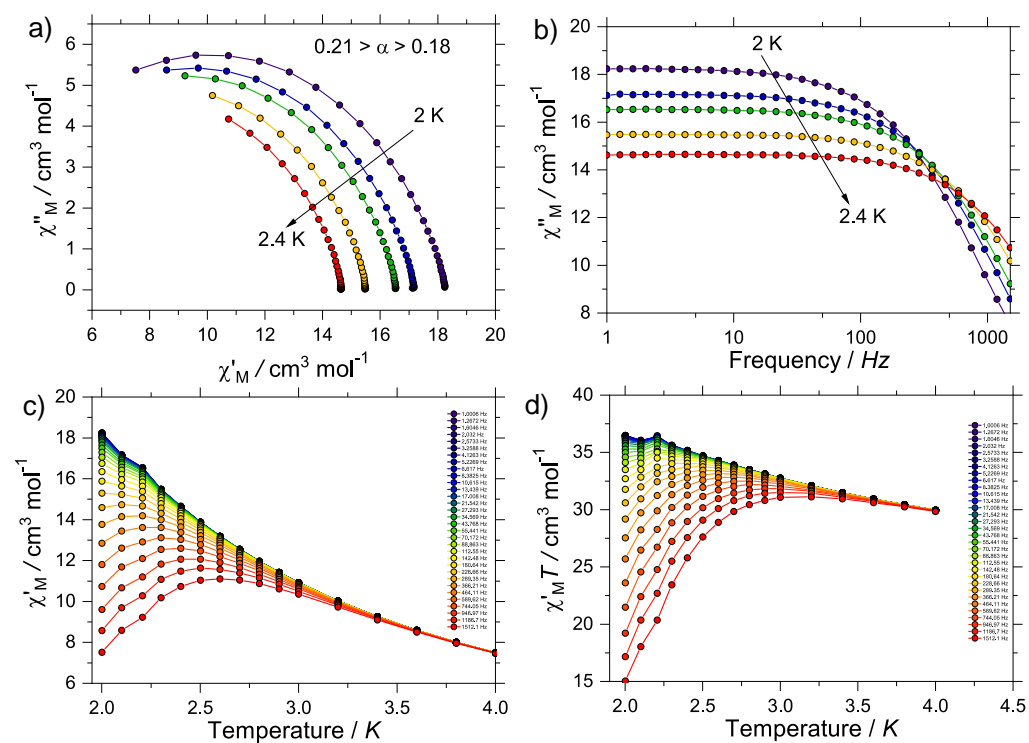


Figure S16. a) Cole-Cole plots for complex **4**; b) Experimental $\chi_M''(\nu)$ with $H_{DC} = 0$ for complex **4**; c) and d) are the experimental $\chi_M'(T)$ and $\chi_M'T(T)$ data for the **Ni₂Mn₂Dy₂** complex.

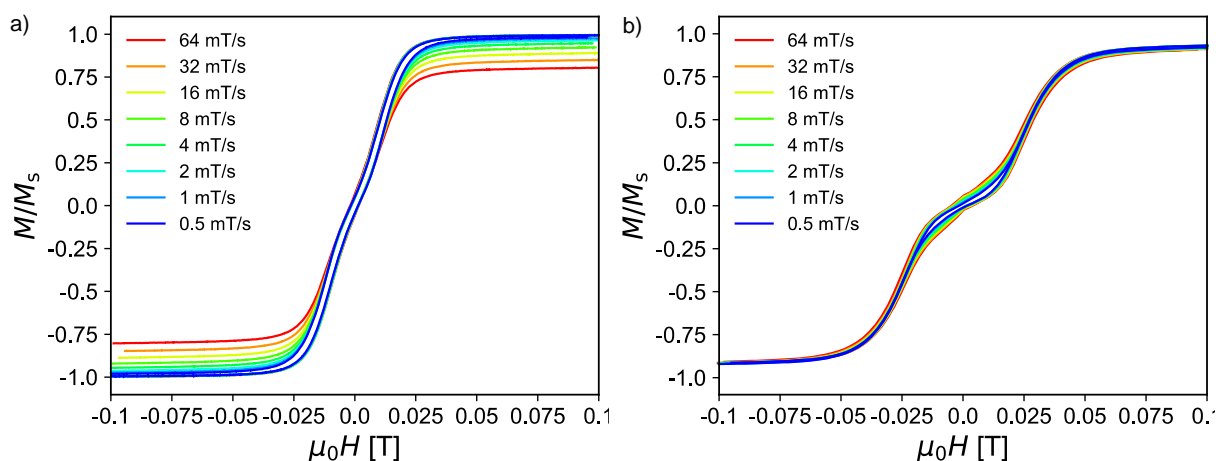


Figure S17. Zoom in of hysteresis loops at 30 mK and different sweep rates for (a) Complex **1** and (b) Complex **4**.

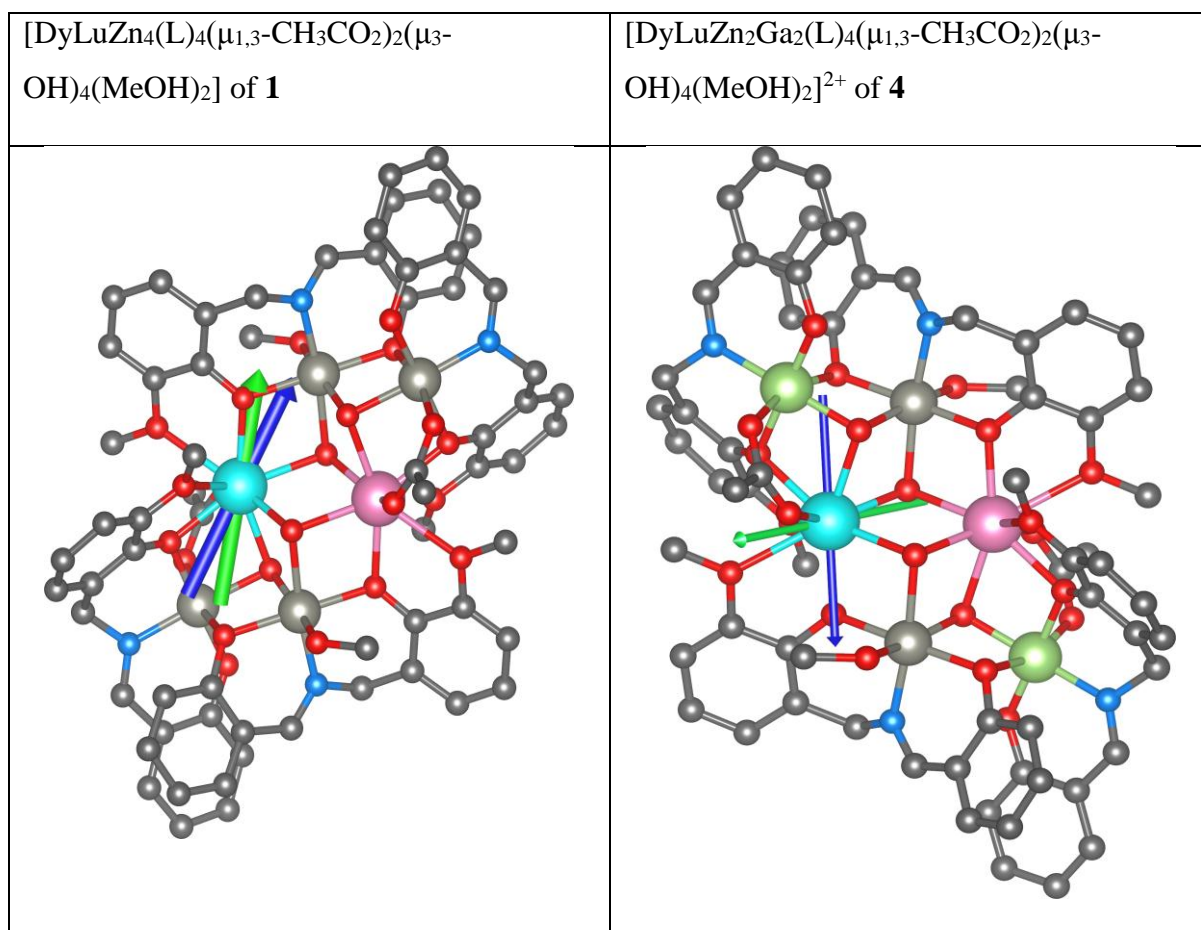


Figure S18. Direction of the principal axis of the g -tensor in the ground Kramers doublet (blue arrow) and in the first excited Kramers doublet (green arrow) for complex **1** and **4**. Hydrogen atoms are omitted for the clarity. Colour code: C, dark grey; N, pale blue; O, red; Zn, grey; Ga, light green; Dy, cyan; Lu, pink.

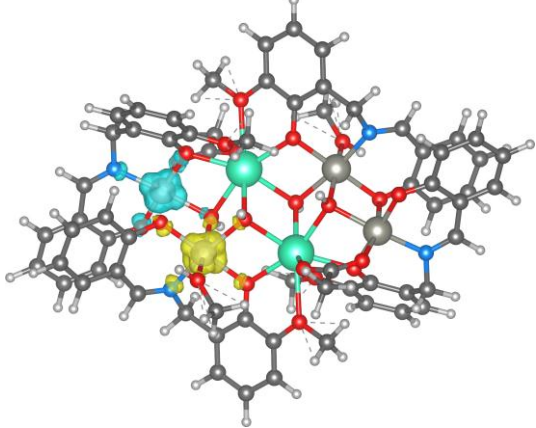
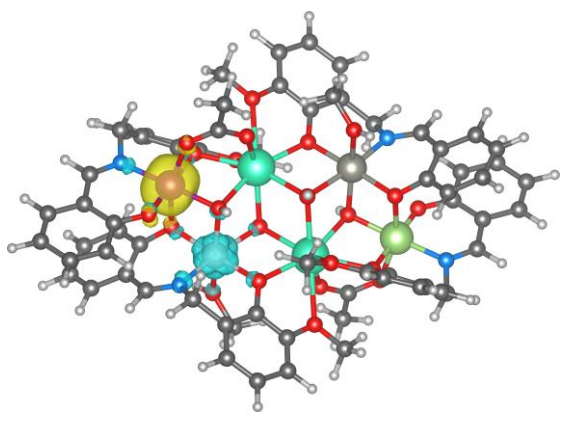
$[\text{Lu}_2\text{Ni}_2\text{Zn}_2(\text{L})_4(\mu_{1,3}\text{-CH}_3\text{CO}_2)_2(\mu_3\text{-OH})_4(\text{MeOH})_2]$ of 1	$[\text{Lu}_2\text{NiMnZnGa}(\text{L})_4(\mu_{1,3}\text{-CH}_3\text{CO}_2)_2(\mu_3\text{-OH})_4(\text{MeOH})_2]^{2+}$ of 4
	
<p>Ni^{II}-Ni^{II} interaction $E(\text{BS})-E(\text{HS})= 32.006 \text{ cm}^{-1}$ $J = +16.0 \text{ cm}^{-1}$ Ferromagnetic isotropic exchange</p>	<p>Ni^{II}-Mn^{III} interaction $E(\text{BS})-E(\text{HS})= -14.889 \text{ cm}^{-1}$ $J = -3.72 \text{ cm}^{-1}$ Antiferromagnetic isotropic exchange</p>

Figure S19. DFT calculated spin densities of BS states in complexes **1** (left) and **4** (right).

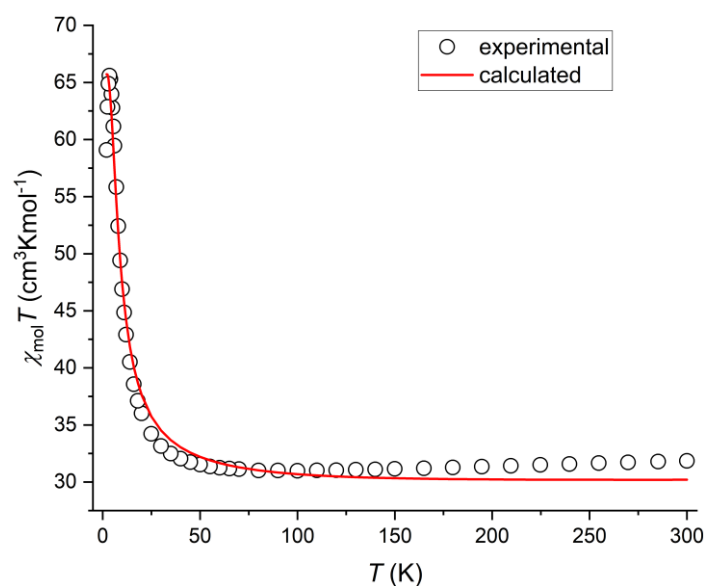


Figure S20. The comparison of the experimental and calculated χT product of **1**. The calculated data were computed with POLY_ANISO module using $J(\text{Ni1-Ni2}) = +16.0 \text{ cm}^{-1}$, $J(\text{Dy1-Dy1}^*) = 0.74 \text{ cm}^{-1}$, $J(\text{Ni1-Dy1}) = -0.87 \text{ cm}^{-1}$ and $J(\text{Ni1-Dy1}^*) = J(\text{Ni2-Dy1}) = 1.40 \text{ cm}^{-1}$ and scaling coefficient 0.89.

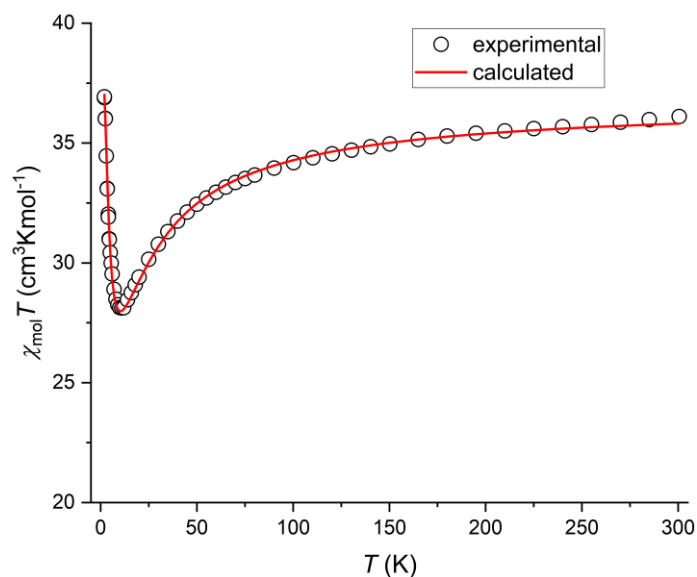


Figure S21. The comparison of the experimental and calculated χT product of **2**. The calculated data were computed with POLY_ANISO module using $J(\text{Ni1-Mn1}) = -3.72 \text{ cm}^{-1}$, $J(\text{Dy1-Dy1}^*) = 0.22 \text{ cm}^{-1}$, $J(\text{Mn1-Dy1}^*) = -1.05 \text{ cm}^{-1}$ and $J(\text{Ni1-Dy1}) = J(\text{Ni1-Dy1}^*) = 0.62 \text{ cm}^{-1}$ and scaling coefficient 0.99.

References

- S1. Pinsky, M.; Avnir, D. Continuous Symmetry Measures. 5. The Classical Polyhedra. *Inorg. Chem.* **1998**, *37*, 5575–5582.
- S2. Alvarez, S.; Avnir, D.; Llunell, M.; Pinsky, M. Continuous symmetry maps and shape classification. The Case of Six-Coordinated Metal Compounds. *New J. Chem.* **2002**, *26*, 996–1009.
- S3. Casanova, D.; Llunell, M.; Alemany, P.; Alvarez, S. The Rich Stereochemistry of Eight-Vertex Polyhedra: A Continuous Shape Measures Study. *Chem. Eur. J.* **2005**, *11*, 1479–1494.